Journal of Computational Physics 485 (2023) 112106

Contents lists available at ScienceDirect

Journal of Computational Physics

journal homepage: www.elsevier.com/locate/jcp

An explicit boundary condition-enforced immersed boundary-reconstructed thermal lattice Boltzmann flux solver for thermal–fluid–structure interaction problems with heat flux boundary conditions

Buchen Wu [a,b], Jinhua Lu [e], HsuChew Lee [b], Chang Shu [a,*], Minping Wan [b,c,d,*]

[a] Department of Mechanical Engineering, National University of Singapore, 10 Kent Ridge Crescent, Singapore, 119260, Singapore
[b] Guangdong Provincial Key Laboratory of Turbulence Research and Applications, Department of Mechanics and Aerospace Engineering, Southern University of Science and Technology, Shenzhen, 518055, Guangdong, China
[c] Guangdong-Hong Kong-Macao Joint Laboratory for Data-Driven Fluid Mechanics and Engineering Applications, Southern University of Science and Technology, Shenzhen, 518055, Guangdong, China
[d] Jiaxing Research Institute, Southern University of Science and Technology, Jiaxing, 314031, Zhejiang, China
[e] Department of Mechanical Engineering, Chair of Aerodynamics and Fluid Mechanics, Technical University of Munich, Boltzmannstraße 15, Garching, 85748, Germany

ARTICLE INFO

Article history:
Received 3 November 2022
Received in revised form 7 March 2023
Accepted 27 March 2023
Available online 5 April 2023

Keywords:
Immersed boundary method
Neumann boundary condition
Reconstructed thermal lattice Boltzmann flux solver

ABSTRACT

For the thermal–fluid–structure interaction (TFSI) problems with moving boundaries, the original implicit boundary condition-enforced immersed boundary method (IBM) by Wang et al. [1] has to generate a large correlation matrix and compute its inversion at each iteration, implying that the virtual memory requirement and computational cost would grow exponentially with the number of Lagrangian points. In this work, we proposed an efficient explicit boundary condition-enforced immersed boundary method for Neumann boundary condition (NBC) to achieve high computational efficiency and maintain similar accuracy as the original implicit IBM [1], which circumvents the needs to assemble a large correlation matrix and inverse it in the original implicit IBM [1] through second-order approximation based on the error analysis using Taylor series expansion. Most importantly, the proposed explicit IBM can efficiently solve practical physics problems with a tremendous amount of Lagrangian points involving Neumann boundary condition. The comparisons of the virtual memory and computational cost between the explicit and implicit IBMs demonstrate that the explicit boundary condition-enforced IBM is not only computational efficient, but also has memory saving performance. The proposed explicit IBM integrated with the reconstructed thermal lattice Boltzmann flux solver (RTLBFS) is validated with some classical benchmarks, and the results show that the proposed explicit IBM can successfully resolve TFSI problems with Neumann boundary condition.

* Corresponding authors.
E-mail addresses: mpeshuc@nus.edu.sg (C. Shu), wanmp@sustech.edu.cn (M. Wan).

https://doi.org/10.1016/j.jcp.2023.112106
0021-9991/

1. Introduction

Thermal-fluid-structure interaction (TFSI) problems are ubiquitous in natural environment and various engineering, such as in industrial cooling systems, chemical processing and nuclear reactor. TFSI problems have always been fascinating yet challenging, where multi-physics coupled effects are involved. Numerous accurate and efficient numerical approaches have been proposed to handle the complex nature of TFSI problems, but the most attractive approach among them is the immersed boundary method (IBM) firstly proposed by Peskin [2], owing to its simplicity and flexibility for tackling complex TFSI problems.

There are generally three types of boundary conditions that can be imposed on solid wall, namely, Dirichlet boundary condition, Neumann boundary condition, and Robin boundary condition. Tremendous efforts have been placed on the Dirichlet boundary condition with many highly accurate and efficient schemes being developed for various IBMs to handle a wide-range of problems involving Dirichlet boundary conditions. For example, the penalty forcing scheme [2,3], the direct forcing scheme [4–8], the feedback forcing scheme [9], the momentum exchange scheme [10–12], and the boundary condition-enforced scheme [13–18]. Peskin [2] proposed the penalty forcing scheme by assuming that the interaction between the solid boundary and fluid satisfies the Hook's law, where the information of structural stiffness is required. However, this parameter is hard to accurately define, thereby it triggers the emergence of the direct forcing scheme [4,7], which requires the explicit evaluation of the restoring force from Navier-Stokes equations. However, conventional IBMs cannot accurately impose the Dirichlet boundary condition on the solid wall by evaluating the restoring force explicitly as it induces unphysical flow penetration into the solid wall. Therefore, Wu and Shu [13] proposed the implicit boundary condition enforced IBM to accurately satisfy Dirichlet boundary condition on the solid boundary. However, the original implicit IBM for Dirichlet boundary condition suffers from tedious matrix generation and complex matrix inversion. Subsequently, Zhao et al. [19] proposed an explicit technique that could eliminate the aforementioned drawbacks, where it has been extensively used to resolve the complex biological propulsion problems [20–22]. These IBMs with Dirichlet boundary condition can easily be extended to simulate TFSI problems with isotherm boundary conditions [23–26].

However, TFSI problems associated with Neumann boundary condition are much more common than Dirichlet boundary condition. Unfortunately, it is much more difficult to develop an IBM approach that could accurately satisfy Neumann boundary condition on solid surface. Zhang et al. [27] attempted to enforce Neumann boundary condition in an explicit direct heating scheme by introducing an auxiliary layer outside the solid boundary. Ren et al. [28] proposed an explicit heat flux correction IBM by determining the difference between the prescribed heat flux and the interpolated heat flux from an intermediate temperature field. Hu et al. [29,30] proposed a numerical scheme derived from the jump condition of the temperature gradient, which is utilized to study the 2D natural convection in an annulus. However, Wang et al. [1] demonstrated that most of the one-step explicit correction-based IBMs cannot accurately satisfy the NBC on the solid boundary, owing to the mutual interaction between the heat sink on the Lagrangian points and the temperature correction on the Eulerian meshes. Therefore, Wang et al. [1] proposed an implicit boundary condition-enforced IBM for Neumann boundary condition with the help of two auxiliary layers inside and outside the immersed boundary, where the heat flux on the solid wall can be obtained by differentiating the local temperature on the two auxiliary layers, thereby, achieving second order accuracy and satisfying Neumann boundary condition on the solid wall. However, the implicit boundary condition-enforced IBM [1] involves large correlation matrix generation and complex matrix inversion to handle the TFSI problems with moving boundary, which puts an enormous amount of pressure on the server memory. Most importantly, the computational cost increases exponentially as the number of Lagrangian points increases.

In this work, to achieve high computational efficiency and maintain similar accuracy as the original implicit IBM [1], we propose an efficient explicit boundary condition-enforced IBM for Neumann boundary condition. The proposed explicit IBM is capable of providing the temperature corrections with second-order accuracy through an error analysis using the Taylor series expansion, without the large correlation matrix generation process and the inversion of the correlation matrix. The proposed explicit IBM is integrated with the RTLBFS for simulating the TFSI problems with Neumann boundary condition. The results from several numerical validations demonstrate that the NBC can be accurately and efficiently satisfied by the proposed explicit IBM. The comparisons of virtual memory and computational time for solving IBM process elucidate the superior performance of the proposed explicit IBM for NBC.

The paper is organized as follows: the governing equations of the fluid dynamics, the numerical approaches for fluid dynamics, and the IBMs for Dirichlet and Neumann boundary conditions are introduced in Section 2. In Section 3.1, the detailed derivation of the explicit IBM for NBC is presented. Subsequently, the comparisons of the virtual memory and computational cost between the explicit and implicit IBMs are performed in Section 3.2. In Section 4, the overall numerical accuracy test and numerical validations of the proposed explicit IBM for NBC are presented. Specifically, Sections 4.2-4.5 demonstrate the capability of the proposed explicit IBM in handling Neumann boundary condition in external and internal thermal flows. Section 4.6 presents the application of the proposed explicit IBM for simulating the 3D TFSI problems with moving boundary. Conclusions are provided in Section 5.

2. The mathematical model and numerical approach

In this section, the governing equations for thermal flows and the numerical approaches are introduced. In the present work, a fractional step method is utilized to simplify the interaction process in TFSI problems. The solution process of a

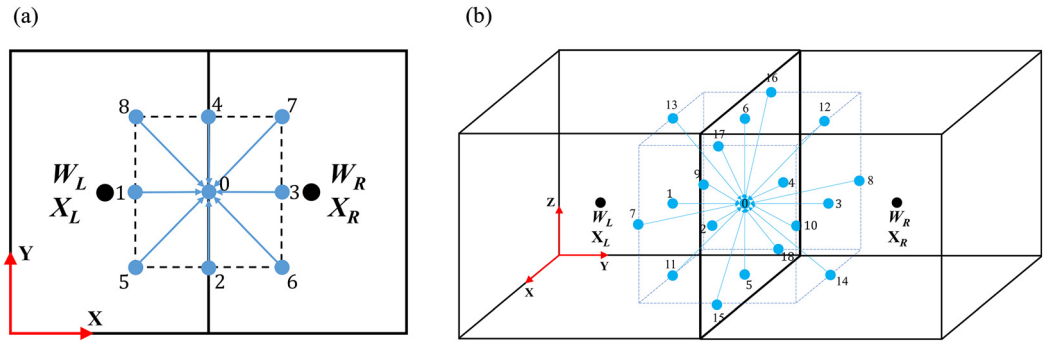

Fig. 1. Local reconstructed unit lattice at the cell interface; (a) D2Q9 and (b) D3Q19. The black points denote the two adjacent cell centers and the blue points denote the unit lattice points. (For interpretation of the colors in the figure(s), the reader is referred to the web version of this article.)

TFSI problem is decomposed into a sequence of two steps (predictor step and corrector step). In the predictor step, the intermediate flow field is predicted by the RTLBFS [31], where the existence of the solid object is not taken into account. Subsequently, in the corrector step, the IBMs for Dirichlet boundary condition and Neumann boundary condition are utilized to resolve the velocity and temperature corrections on the solid wall, respectively.

2.1. Navier-Stokes (N-S) equations

For thermal viscous flows, the Navier-Stokes (N-S) equations of the mass, momentum and energy conservation can be expressed as:

$$\frac{\partial \rho}{\partial t} + \nabla \cdot (\rho \mathbf{u}) = 0, \tag{1a}$$

$$\frac{\partial (\rho \mathbf{u})}{\partial t} + \nabla \cdot (\rho \mathbf{u}\mathbf{u}) = -\nabla p + \nu \nabla \cdot \left[\nabla \rho \mathbf{u} + (\nabla \rho \mathbf{u})^T\right] + \mathbf{F}_B + \mathbf{f}, \tag{1b}$$

$$\frac{\partial \left(\rho c_p T\right)}{\partial t} + \nabla \cdot (\rho c_p T \mathbf{u}) = \chi \nabla^2 (\rho c_p T) + q, \tag{1c}$$

where ρ is the fluid density, $\mathbf{u}$ is the flow velocity, T denotes the temperature. ν, p, c_p and χ denote the kinematic viscosity, the pressure, the specific heat capacity at constant pressure, and the thermal diffusivity, respectively. Based on the Boussinesq approximation, the buoyancy force can be evaluated as $\mathbf{F}_B = (0, 0, -\rho\zeta g(T - T_m))$, where ζ, g and T_m are the thermal expansion coefficient, gravitational acceleration and averaged temperature, respectively. $\mathbf{f}$ and q denote the restoring forcing term and the heat source term, respectively. The above N-S equations can simulate the incompressible thermal viscous flow, provided that the density variation is small and Mach number is low.

2.2. The RTLBFS for determining the intermediate flow variables

In the predictor step, the standard N-S equations are solved with the RTLBFS without considering the presence of the solid domain, hence, the restoring forcing term $\mathbf{f}$ and the heat source term q in Eqs. (1b) and (1c) are set to zero in present step. The governing equations shown in Eq. (1) can be rewritten in a vector form:

$$\frac{\partial \mathbf{W}}{\partial t} + \nabla \cdot \mathbf{F} = 0, \tag{2}$$

where

$$\mathbf{W} = \begin{Bmatrix} \rho \\ \rho \mathbf{u} \\ \rho c_p T \end{Bmatrix}, \quad \mathbf{F} = \begin{Bmatrix} \mathbf{P} \\ \mathbf{\Pi} \\ \mathbf{Q} \end{Bmatrix}, \tag{3a}$$

$$\boldsymbol{P} = \rho \mathbf{u}, \tag{3b}$$

$$\mathbf{\Pi} = \rho \mathbf{u}\mathbf{u} + p\boldsymbol{I} - \nu \left(\nabla \rho \mathbf{u} + (\nabla \rho \mathbf{u})^T\right), \tag{3c}$$

$$\mathbf{Q} = \rho c_p T \mathbf{u} - \chi \nabla (\rho c_p T). \tag{3d}$$

It is worth mentioning here that the buoyancy force $\mathbf{F}_B$ is considered in the intermediate step shown in Eq. (7) rather than in the flux term $\mathbf{\Pi}$.

Firstly, a unit lattice is constructed at the cell interface with the lattice velocity model shown in Fig. 1. Then, the macroscopic flow variables $\mathbf{W} = (\rho, \mathbf{u}, T)$ at each lattice node are approximately evaluated with the following interpolation scheme:

$$\mathbf{W} = \begin{cases} \mathbf{W}_L + \nabla \mathbf{W}_L \cdot (\mathbf{X}_N - \mathbf{X}_L), \mathbf{X}_N \text{ locates at the left cell;} \\ \mathbf{W}_R + \nabla \mathbf{W}_R \cdot (\mathbf{X}_N - \mathbf{X}_R), \mathbf{X}_N \text{ locates at the right cell;} \\ 0.5\left[\mathbf{W}_L + \nabla \mathbf{W}_L \cdot (\mathbf{X}_N - \mathbf{X}_L) + \mathbf{W}_R + \nabla \mathbf{W}_R \cdot (\mathbf{X}_N - \mathbf{X}_R)\right], \\ \qquad\qquad \mathbf{X}_N \text{ locates at the interface;} \end{cases} \tag{4}$$

where $\mathbf{X}_L$ and $\mathbf{X}_R$ are the cell center position of the two adjacent cells. In the present work, the superscripts n, $*$, m and $n+1$ denote the current, the sub-intermediate, the intermediate and the next time steps, respectively.

Subsequently, the sub-intermediate macroscopic flow variables at the cell interface are evaluated through solving the macroscopic equations, which is recovered from the local thermal LBM with the finite difference method, as follows:

$$\rho^* = \rho^n - \partial_\alpha (\rho u_\alpha)^n \delta t + \frac{1}{2}\delta t^2 \partial_\alpha \partial_\beta \left(\rho u_\alpha u_\beta + \rho c_s^2 \delta_{\alpha\beta}\right)^n + O\left(\delta t^3\right), \tag{5a}$$

$$(\rho u_\alpha)^* = (\rho u_\alpha)^n - \delta t \partial_\beta \left(\rho u_\alpha u_\beta + \rho c_s^2 \delta_{\alpha\beta}\right)^n + 0.5 c_s^2 \delta t^2 \partial_\beta \left[\partial_\beta (\rho u_\alpha) + \partial_\alpha (\rho u_\beta) + \partial_\gamma (\rho u_\gamma)\delta_{\alpha\beta}\right]^n + O\left(\delta t^3\right), \tag{5b}$$

$$(\rho c_p T)^* = (\rho c_p T)^n - \delta t \partial_\alpha (\rho c_p u_\alpha T)^n + 0.5 c_s^2 \delta t^2 \partial_\alpha \partial_\beta (\rho c_p T \delta_{\alpha\beta})^n + O\left(\delta t^3\right), \tag{5c}$$

where subscripts α, β and γ are the coordinate components. c_s denotes the speed of sound and δt is the time interval. The partial derivatives in Eq. (5) are discretized on the unit lattice using the second-order central difference scheme [32].

Using the second-order Taylor series expansion [31], the flux terms in Eq. (3a) can be obtained by invoking the sub-intermediate macroscopic variables, which can be expressed as:

$$P_\alpha = (\rho u_\alpha)^*, \tag{6a}$$

$$\begin{aligned} \Pi_{\alpha\beta} = &\left(\rho u_\alpha u_\beta + \rho c_s^2 \delta_{\alpha\beta}\right)^* - \nu\left[\partial_\beta (\rho u_\alpha) + \partial_\alpha (\rho u_\beta) + \partial_\gamma (\rho u_\gamma)\delta_{\alpha\beta}\right] \\ &- (\tau_f - 0.5)\left[\left(\rho u_\alpha u_\beta + \rho c_s^2 \delta_{\alpha\beta}\right)^* - \left(\rho u_\alpha u_\beta + \rho c_s^2 \delta_{\alpha\beta}\right)\right] + O\left(\delta t^2\right), \end{aligned} \tag{6b}$$

$$Q_\alpha = (\rho c_p u_\alpha T)^* - \chi \partial_\alpha (\rho c_p T) - (\tau_g - 0.5)\left[(\rho c_p u_\alpha T)^* - (\rho c_p u_\alpha T)\right] + O\left(\delta t^2\right), \tag{6c}$$

where τ_f and τ_g are the relaxation parameters, which are related to the kinematic viscosity $\nu = (\tau_f - 0.5) c_s^2 \delta t$ and thermal diffusivity coefficient $\chi = (\tau_g - 0.5) c_s^2 \delta t$, respectively.

Finally, the macroscopic flow variables ρ^{n+1}, $\mathbf{u}^m$, and T^m at the cell center are computed with the flux terms as follows:

$$\rho^{n+1} = \rho^n - \frac{\Delta t}{\Delta V} \sum_k P_\alpha \Delta S_{k\alpha}, \tag{7a}$$

$$(\rho u_\alpha)^m = (\rho u_\alpha)^n + \frac{\Delta t}{\Delta V} \sum_k \Pi_{\alpha\beta} \Delta S_{k\beta} + F_{B\alpha}, \tag{7b}$$

$$(\rho c_p T)^m = (\rho c_p T)^n - \frac{\Delta t}{\Delta V} \sum_k Q_\alpha \Delta S_{k\alpha}, \tag{7c}$$

where ΔV denotes the control cell's volume and Δt is the macroscopic time interval. ΔS_k denotes the area of the kth interface of the control cell.

2.3. Velocity corrections obtained by the IBM for Dirichlet boundary condition

For simplicity, the two-dimensional methodology of IBM is presented. To satisfy the no-slip boundary condition, the boundary condition-enforced immersed boundary method with explicit technique is applied to correct the intermediate velocity field [26]. The velocity corrections can be evaluated with the following scheme:

$$\Delta \mathbf{u} = \mathbf{u}^{n+1} - \mathbf{u}^m, \tag{8}$$

where $\Delta \mathbf{u}$ denotes the corresponding corrections on the velocity field. Therefore, the restoring forcing terms in the momentum equation can be expressed as:

$$\mathbf{f} = \rho^{n+1} \frac{\Delta \mathbf{u}}{\Delta t}. \tag{9}$$

For simplicity, the symbol ψ is adopted to represent the two velocity components, thus, Eq. (8) can be rewritten as:

$$\psi^{n+1} = \psi^m + \Delta\psi. \tag{10}$$

The difference between the local flow velocity and the desired velocity on the solid wall needs to be eliminated to accurately impose the no-slip boundary conditions, which can be expressed as:

$$\begin{aligned} &\psi_B\left(\boldsymbol{X}_B^l\right) = \psi^{n+1}\left(\boldsymbol{X}_B^l\right) = \sum_j \psi^{n+1}\left(\boldsymbol{r}_j\right) \cdot D\left(\boldsymbol{r}_j - \boldsymbol{X}_B^l\right) h^2 \\ &l = 1, 2, \ldots, N, \quad j = 1, 2, \ldots, M \end{aligned} \tag{11}$$

where the subscript B denotes the Lagrangian points on the solid wall. h is the background Eulerian mesh spacing; N and M denote the numbers of Lagrangian points and Eulerian points, respectively. $\boldsymbol{r}_j$ represent the physical position of Eulerian points. The kernel distribution function D can be written as:

$$D\left(\boldsymbol{r}_j - \boldsymbol{X}_B^l\right) = \delta\left(r_j^x - X_B^l\right)\delta\left(r_j^y - Y_B^l\right), \tag{12}$$

$$\delta(r) = \begin{cases} \left[1 + \sqrt{1 - 3(r/h)^2}\right]/3, & |r| \le 0.5h, \\ \left[5 - 3|r|/h - \sqrt{1 - 3(1 - |r|/h)^2}\right]/6, & 0.5h < |r| \le 1.5h, \\ 0, & |r| > 1.5h. \end{cases} \tag{13}$$

The correction $\Delta\psi(\boldsymbol{r}_j)$ at Eulerian points can be obtained through the interpolation with the correction $\delta\psi_B^l$ at Lagrangian points as follows:

$$\Delta\psi\left(\boldsymbol{r}_j\right) = \sum_l \delta\psi_B^l \cdot D\left(\boldsymbol{r}_j - \boldsymbol{X}_B^l\right) \cdot \Delta s^l, l = 1, 2, \ldots, N, \tag{14}$$

where Δs^l represents the arc length of the solid boundary element. Substituting Eqs. (10) and (14) into Eq. (11), the following relationship can be obtained as:

$$\psi_B\left(\boldsymbol{X}_B^l\right) = \sum_j \psi^m\left(\boldsymbol{r}_j\right) \cdot D\left(\boldsymbol{r}_j - \boldsymbol{X}_B^l\right) h^2 + \sum_j \sum_k \delta\psi_B^k \Delta s^k \cdot D\left(\boldsymbol{r}_j - \boldsymbol{X}_B^l\right) \cdot D\left(\boldsymbol{r}_j - \boldsymbol{X}_B^k\right) h^2. \tag{15}$$

Equation (15) can be rewritten in the matrix form as follows:

$$\mathbf{A}\boldsymbol{x} = \mathbf{B} \tag{16a}$$

$$\boldsymbol{x} = \left[\, \delta\psi_B^1 \Delta s^1, \quad \delta\psi_B^2 \Delta s^2, \quad \cdots, \quad \delta\psi_B^N \Delta s^N \,\right]^T, \tag{16b}$$

$$A_{ij} = \sum_{k=1}^{M} D_{ik} D_{jk} h^2, \tag{16c}$$

$$B_i = \psi_B^i - \sum_{k=1}^{M} D_{ik} \psi_k^m. \tag{16d}$$

By solving the linear equation system of Eq. (16a) with an explicit technique [19], the unknown term $\delta\psi_B^i \Delta s^i$ on the Lagrangian points can be obtained.

2.4. Temperature corrections obtained by the original IBM for Neumann boundary condition

In this subsection, the original implicit boundary condition-enforced immersed boundary method for Neumann boundary condition [1] is introduced. The implicit IBM is applied in the corrector step, right after the intermediate temperature field is evaluated, to accurately satisfy the Neumann boundary conditions on the solid wall. The corrected temperature is obtained by accounting for the corrections as follows:

$$T^{n+1} = T^m + \Delta T, \tag{17}$$

where ΔT denotes the temperature correction. Therefore, the source term in the energy equation can be expressed as:

$$q = \rho^{n+1} c_p \frac{\Delta T}{\Delta t}. \tag{18}$$

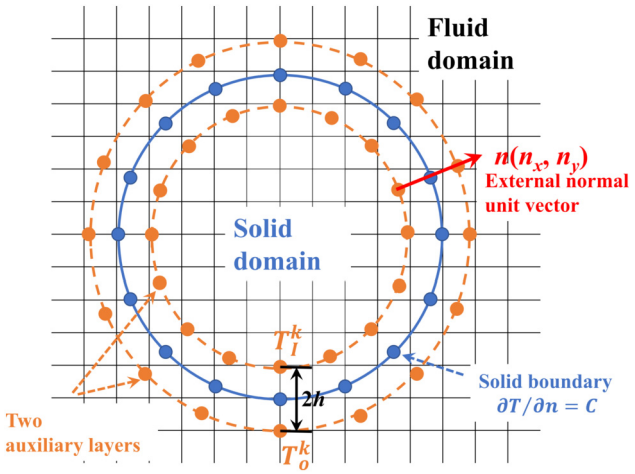

Fig. 2. Illustration of the immersed boundary method for Neumann boundary condition.

Fig. 2 shows the scheme of the IBM for Neumann boundary condition, where two auxiliary layers are placed inside and outside of the solid boundary with a distance of $2h$. Based on the central difference scheme, the heat flux with the second order of accuracy at the Lagrangian points on the surface of the solid domain can be obtained by:

$$\frac{\partial T^k}{\partial n} = \frac{1}{2h}\left(T_O^k - T_I^k\right), \tag{19}$$

where T_O^k and T_I^k denote the kth temperature on the outer and inner auxiliary layers, respectively, which can be evaluated by:

$$T_O^k = T_O^{mk} + \delta T_O^k, \tag{20a}$$

$$T_I^k = T_I^{mk} + \delta T_I^k, \tag{20b}$$

where T_O^{mk} and T_I^{mk} are the intermediate temperatures on the outer and inner layers, which can be obtained by:

$$T_O^{mk}\left(\boldsymbol{X}_O\right) = \sum_j T^m\left(\boldsymbol{x}_j\right) \cdot D\left(\boldsymbol{x}_j - \boldsymbol{X}_O^k\right) \cdot h^2, \tag{21a}$$

$$T_I^{mk}\left(\boldsymbol{X}_I\right) = \sum_j T^m\left(\boldsymbol{x}_j\right) \cdot D\left(\boldsymbol{x}_j - \boldsymbol{X}_I^k\right) \cdot h^2. \tag{21b}$$

Similarly, the temperature corrections on the auxiliary layers can be evaluated by the following interpolation relationships:

$$\delta T_O^k\left(\boldsymbol{X}_O\right) = \sum_j \Delta T\left(\boldsymbol{x}_j\right) \cdot D\left(\boldsymbol{x}_j - \boldsymbol{X}_O^k\right) \cdot h^2, \tag{22a}$$

$$\delta T_I^k\left(\boldsymbol{X}_I\right) = \sum_j \Delta T\left(\boldsymbol{x}_j\right) \cdot D\left(\boldsymbol{x}_j - \boldsymbol{X}_I^k\right) \cdot h^2. \tag{22b}$$

Substituting Eqs. (20) and (21) into Eq. (19), the following relationship is obtained as:

$$2h\frac{\partial T^k}{\partial n} = T_O^k - T_I^k = T_O^{mk} - T_I^{mk} + \delta T_O^k\left(\boldsymbol{X}_O\right) - \delta T_I^k\left(\boldsymbol{X}_I\right). \tag{23}$$

Differing from the double-sided distribution corrected source in the Section 2.3, the biased distribution is implemented in the temperature field, because the diffusion introduced by the smooth delta function would pollute the temperature field outside the solid domain. Therefore, the temperature correction on the inner layer is adopted as the heat source, which is only distributed to the field inside the inner layer. This relationship can be expressed as:

$$\Delta T\left(\boldsymbol{x}_j\right) = \begin{cases} \sum_k \left(\delta T_I^k\right) \cdot D\left(\boldsymbol{x}_j - \boldsymbol{X}_I^k\right) \cdot \Delta s_I^k, & \text{for } \boldsymbol{x}_j \text{ inside the inner layer;} \\ 0, & \text{elsewhere.} \end{cases} \tag{24}$$

Substituting Eqs. (22) and (24) into Eq. (23) yields:

$$\begin{aligned} 2h\frac{\partial T^k}{\partial n} &= T_O^{mk} - T_I^{mk} + \sum_j \Delta T\left(\boldsymbol{x}_j\right)\cdot\left(D\left(\boldsymbol{x}_j - \boldsymbol{X}_O^k\right) - D\left(\boldsymbol{x}_j - \boldsymbol{X}_I^k\right)\right)\cdot h^2 \\ &= T_O^{mk} - T_I^{mk} + \sum_j \left(\sum_l \left(\delta T_I^l \cdot \Delta s^l\right)\cdot D\left(\boldsymbol{x}_j - \boldsymbol{X}_I^l\right)\right)\cdot\left(D\left(\boldsymbol{x}_j - \boldsymbol{X}_O^k\right) - D\left(\boldsymbol{x}_j - \boldsymbol{X}_I^k\right)\right)\cdot h^2, \end{aligned} \tag{25}$$

which can be rewritten in the matrix form as follows:

$$\boldsymbol{C}\boldsymbol{Y} = \boldsymbol{E} \tag{26a}$$

$$C_{kl} = \sum_j \left[D\left(\boldsymbol{x}_j - \boldsymbol{X}_I^l\right)\cdot\left(D\left(\boldsymbol{x}_j - \boldsymbol{X}_O^k\right) - D\left(\boldsymbol{x}_j - \boldsymbol{X}_I^k\right)\right)\right]\cdot h^2 \tag{26b}$$

$$\boldsymbol{E} = \left[2h\frac{\partial T^1}{\partial n} - T_O^{m1} + T_I^{m1}, \ldots, 2h\frac{\partial T^k}{\partial n} - T_O^{mk} + T_I^{mk}, \ldots, 2h\frac{\partial T^N}{\partial n} - T_O^{mN} + T_I^{mN}\right]^t \tag{26c}$$

$$\boldsymbol{Y} = \left[\delta T_I^1 \cdot \Delta s^1, \ldots, \delta T_I^l \cdot \Delta s^l, \ldots, \delta T_I^N \cdot \Delta s^N\right]^t \tag{26d}$$

The procedure of the original implicit IBM for Neumann boundary condition is summarized in Algorithm 1. In the implicit IBM for Neumann boundary condition [1], the assembly and inversion of matrix $\boldsymbol{C}$ requires large virtual memory and high computational cost when a large number of Lagrangian points are involved. Especially, when the moving boundary is involved in the TFSI problems, the matrix $\boldsymbol{C}$ and its inversion need to be updated at each time step.

Algorithm 1 The implicit IBM for Neumann boundary condition.

Step 1: $\boldsymbol{D_O}$ and $\boldsymbol{D_I}$
Step 2: $\boldsymbol{C} = \boldsymbol{D_I}\cdot(\boldsymbol{D_O} - \boldsymbol{D_I})$
Step 3: $\boldsymbol{C}^{-1} = \frac{1}{|\boldsymbol{C}|}\begin{bmatrix} C_{11} & C_{21} & \ldots & C_{N1} \\ C_{12} & C_{22} & \ldots & C_{N2} \\ \ldots & \ldots & \ldots & \ldots \\ C_{1N} & C_{2N} & \ldots & C_{NN} \end{bmatrix}$
Step 4: $\boldsymbol{Y} = \boldsymbol{C^{-1}E}$
Step 5: $T^{n+1} = T^m + \boldsymbol{D_I^t Y}$

3. The explicit boundary condition-enforced immersed boundary method for Neumann boundary conditions

In this section, the explicit technique is firstly proposed to simplify the tedious matrix generation process and the complex matrix inversion required by the original implicit boundary condition-enforced IBM for ensuring the NBC. The explicit technique is developed through error analysis with the help of Taylor series expansion, and a second-order approximation is derived. Subsequently, the comparisons of the virtual memory and computational cost between the explicit and implicit IBMs are performed.

3.1. The derivation of the explicit technique

The detailed derivation of the explicit technique is presented in this subsection. Recalling Eq. (26) from previous section, the matrix form can be rewritten as:

$$\sum_{l=1}^{N} C_{kl}\delta T_I^l\left(\boldsymbol{X}_I^l\right)\Delta s^l = \boldsymbol{E}_k. \tag{27}$$

The unknown term $\delta T_I^l\left(\boldsymbol{X}_l\right)\Delta s^l$ is related to the $\boldsymbol{E}_k$ when the coefficient $C_{kl} \neq 0$. Hence, Eq. (27) can be rewritten as:

$$\sum_{l\in\{C_{kl}\neq 0\}} C_{kl}\delta T_I^l\left(\boldsymbol{X}_I^l\right)\Delta s^l = \boldsymbol{E}_k \tag{28}$$

The relationship $C_{kl} \neq 0$ requires:

$$D\left(\boldsymbol{x}_j - \boldsymbol{X}_I^l\right) \neq 0, \tag{29a}$$

$$D\left(\boldsymbol{x}_j - \boldsymbol{X}_O^k\right) \neq D\left(\boldsymbol{x}_j - \boldsymbol{X}_I^k\right). \tag{29b}$$

As described previously (see Eq. (24)), the temperature correction only exists on the Eulerian points $\boldsymbol{x}_j$, which locates inside the inner auxiliary layer, indicating that $D\left(\boldsymbol{x}_j - \boldsymbol{X}_O^k\right) \leq D\left(\boldsymbol{x}_j - \boldsymbol{X}_I^k\right)$. Only when $D\left(\boldsymbol{x}_j - \boldsymbol{X}_O^k\right) = 0$ and $D\left(\boldsymbol{x}_j - \boldsymbol{X}_I^k\right) = 0$, the $D\left(\boldsymbol{x}_j - \boldsymbol{X}_O^k\right) = D\left(\boldsymbol{x}_j - \boldsymbol{X}_I^k\right)$. With this relationship, the Eq. (29b) can be satisfied with $D\left(\boldsymbol{x}_j - \boldsymbol{X}_I^k\right) \neq 0$.

Assuming the Eulerian grid $j \in S(l)$, the relationship $D\left(\boldsymbol{x}_j - \boldsymbol{X}_I^l\right) \neq 0$ can be satisfied. Similarly, $D\left(\boldsymbol{x}_j - \boldsymbol{X}_I^k\right) \neq 0$ can be achieved when the Eulerian grid $j \in S(k)$. $C_{kl} \neq 0$ requires the Lagrangian points l and k to share the common Eulerian grids $j \in S(l) \cap S(k)$. With the delta function, when $j \in S(l)$, $\left\|\boldsymbol{x}_j - \boldsymbol{X}_I^l\right\| \leq \left\|(1.5h, 1.5h, 1.5h)^t\right\| = O(h)$. Similarly, when $j \in S(k)$, $\left\|\boldsymbol{x}_j - \boldsymbol{X}_I^k\right\| \leq \left\|(1.5h, 1.5h, 1.5h)^t\right\| = O(h)$.

Therefore, to ensure $C_{kl} \neq 0$, the distance between Lagrangian points should satisfy the following relationship:

$$\begin{aligned}\left\|d\boldsymbol{X}_I^{kl}\right\| &= \left\|\boldsymbol{X}_I^l - \boldsymbol{X}_I^k\right\| \\ &= \left\|\left(\boldsymbol{x}_j - \boldsymbol{X}_I^k\right) - \left(\boldsymbol{x}_j - \boldsymbol{X}_I^l\right)\right\| \\ &\leq \left\|\boldsymbol{x}_j - \boldsymbol{X}_I^k\right\| + \left\|\boldsymbol{x}_j - \boldsymbol{X}_I^l\right\| \\ &\leq \left\|(3h, 3h, 3h)^T\right\| \\ &= O(h)\end{aligned} \tag{30}$$

Through the second-order Taylor series expansion, the terms $\delta T_I^l\left(\boldsymbol{X}_I^l\right)$ and Δs^l can be expanded as:

$$\delta T_I^l\left(\boldsymbol{X}_I^l\right) = \delta T_I^k\left(\boldsymbol{X}_I^k\right) + \frac{\partial \delta T_I}{\partial \boldsymbol{X}} d\boldsymbol{X}_I^{kl} + O\left(d\boldsymbol{X}_I^{kl2}\right) \tag{31}$$

$$\Delta s^l = \Delta s^k + \frac{\partial \Delta s}{\partial \boldsymbol{X}} d\boldsymbol{X}_I^{kl} + O\left(d\boldsymbol{X}_I^{kl2}\right) \tag{32}$$

Multiplying Eqs. (31) and (32) gives:

$$\begin{aligned}\delta T_I^l\left(\boldsymbol{X}_I^l\right)\Delta s^l = {} & \delta T_I^k\left(\boldsymbol{X}_I^k\right)\Delta s^k + \frac{\partial \delta T_I}{\partial \boldsymbol{X}} d\boldsymbol{X}_I^{kl}\Delta s^k + \frac{\partial \Delta s}{\partial \boldsymbol{X}} d\boldsymbol{X}_I^{kl}\delta T_I^k\left(\boldsymbol{X}_I^k\right) \\ & + \frac{\partial \delta T_I}{\partial X}\frac{\partial \Delta s}{\partial \boldsymbol{X}} d\boldsymbol{X}_I^{kl} d\boldsymbol{X}_I^{kl} + \Delta s^k O\left(d\boldsymbol{X}_I^{kl2}\right) + \delta T_I^k\left(\boldsymbol{X}_I^k\right) O\left(d\boldsymbol{X}_I^{kl2}\right) + O\left(d\boldsymbol{X}_I^{kl3}\right) \\ = {} & \delta T_I^k\left(\boldsymbol{X}_I^k\right)\Delta s^k + \frac{\partial \delta T_I}{\partial \boldsymbol{X}} d\boldsymbol{X}_I^{kl}\Delta s^k + \frac{\partial \Delta s}{\partial \boldsymbol{X}} d\boldsymbol{X}_I^{kl}\delta T_I^k\left(\boldsymbol{X}_I^k\right) + O\left(d\boldsymbol{X}_I^{kl2}\right)\end{aligned} \tag{33}$$

where Δs^k denotes the spacing of the auxiliary Lagrangian points on the inner auxiliary layer. To establish a proper correlation between Lagrangian points and Eulerian grids, Δs^k requires:

$$\Delta s^k = O(h) \tag{34}$$

In addition, $\delta T_I = q\Delta t$ is related to the time step Δt, yielding:

$$\delta T_I = O(\Delta t) = O(CFL \cdot h) = O(h), \tag{35}$$

where CFL denotes the Courant–Friedrichs–Lewy number. By substituting these two relations into Eq. (33), the second and third terms in Eq. (33) can be simplified as:

$$\begin{aligned}\left\|\frac{\partial \delta T_I}{\partial \boldsymbol{X}} d\boldsymbol{X}_I^{kl}\Delta s^k\right\| &\leq \left\|\frac{\partial \delta T_I}{\partial \boldsymbol{X}}\right\| \left\|d\boldsymbol{X}_I^{kl}\right\| \left\|\Delta s^k\right\| \\ &= \left\|\frac{\partial \delta T_I}{\partial \boldsymbol{X}}\right\| \cdot O(h) \cdot O(h) \\ &= O\left(h^2\right)\end{aligned} \tag{36}$$

$$\begin{aligned}\left\|\frac{\partial \Delta s}{\partial \boldsymbol{X}} d\boldsymbol{X}_I^{kl}\delta T_I^k\left(\boldsymbol{X}_I^k\right)\right\| &\leq \left\|\frac{\partial \Delta s}{\partial \boldsymbol{X}}\right\| \left\|d\boldsymbol{X}_I^{kl}\right\| \left\|\delta T_I^k\left(\boldsymbol{X}_I^k\right)\right\| \\ &= \left\|\frac{\partial \Delta s}{\partial \boldsymbol{X}}\right\| \cdot O(h) \cdot O(h) \\ &= O\left(h^2\right)\end{aligned} \tag{37}$$

Substituting Eqs. (36) and (37) into Eq. (33), Eq. (33) can be simplified as:

Table 1
Comparison of the virtual memory for storing the variables related to IBM of implicit and explicit IBMs for Neumann boundary condition.

Number of Lagrangian points	Algorithm		Ratio
	Implicit IBM	Explicit IBM	
1000	7.6294 MB	7.8125 KB	1000
5000	190.7349 MB	39.0625 KB	5000
10000	762.9395 MB	78.125 KB	10000
15000	1716.6138 MB	117.1875 KB	15000
20000	3051.7578 MB	156.25 KB	20000

Table 2
Comparison of the time consumption for solving the IBM of implicit and explicit IBMs for Neumann boundary condition with one CPU core (2.3 GHz).

Number of Lagrangian points	Algorithm		Ratio
	Implicit IBM	Explicit IBM	
1000	23.6406 s	19.2969 s	1.225
5000	1515.2500 s	104.0781 s	14.559
10000	13865.6563 s	223.6250 s	62.004
15000	90277.5938 s	373.1406 s	241.940
20000	216872.1250 s	523.2813 s	414.447

$$\delta T_I^l\left(\boldsymbol{X}_I^l\right)\Delta s^l = \delta T_I^k\left(\boldsymbol{X}_I^k\right)\Delta s^k + O\left(h^2\right) \tag{38}$$

With the above relation and the definition of $\boldsymbol{\Upsilon}_k = \sum_{l\in\{C_{kl}\neq 0\}} C_{kl}$, Eq. (28) can be rewritten as:

$$\delta T_I^k\left(\boldsymbol{X}_I^k\right)\Delta s^k = \frac{\boldsymbol{E}_k}{\boldsymbol{\Upsilon}_k} \tag{39}$$

The procedure of explicit IBM for Neumann boundary condition is summarized in Algorithm 2. As shown in Eq. (38), the

Algorithm 2 The explicit IBM for Neumann boundary condition.

Step 1: $\boldsymbol{D_O}$ and $\boldsymbol{D_I}$
Step 2: $\boldsymbol{\Upsilon_k} = \sum_I \sum_j [D_I \cdot (D_O - D_I)]$
Step 3: $\boldsymbol{Y} = \boldsymbol{E}/\boldsymbol{\Upsilon}$
Step 4: $T^{n+1} = T^m + \boldsymbol{D_I^t Y}$

second order approximation is preserved in the explicit IBM for Neumann boundary condition. Since RTLBFS utilized in the present work is of second order accuracy, the overall accuracy will not be affected by such approximation.

3.2. Comparisons of the virtual memory and computational cost between implicit and explicit IBMs for Neumann boundary condition

For three-dimensional TFSI problems related to the Neumann boundary condition, large Lagrangian points are required to establish a proper correlation between Lagrangian points and Eulerian meshes. Therefore, the original implicit IBM [1] for NBC demands a large virtual memory for storing the correlation matrix and huge computational effort for matrix inversion. The original implicit IBM and proposed explicit IBM in this work are compared in terms of virtual memory and computational cost at various number of Lagrangian points.

In this test, the size of the Eulerian meshes is 200^3 and the number of the Lagrangian points varies from 10^3 to 2×10^4. The comparisons related to the virtual memory requirement and computational time between the implicit IBM and the proposed explicit IBM are presented in Table 1 and Table 2, respectively. From Table 1, it can be seen that the implicit IBM requires N times virtual memory more than that of the proposed explicit IBM, highlighting the practicability of explicit IBM for solving practical physical problems. As shown in Table 2, the proposed explicit IBM is far more efficient than the implicit IBM when the number of Lagrangian points exceeds 10^3, which demonstrates that the proposed explicit IBM can efficiently tackle the TFSI problems related to the Neumann boundary condition.

4. Results and discussion

In this section, the overall numerical accuracy of the proposed explicit boundary condition-enforced immersed boundary method for Neumann boundary condition integrated with RTLBFS is evaluated with the transient heat diffusion of a Gaussian hill. Subsequently, the robustness and suitability of the proposed explicit IBM for Neumann boundary condition are validated with external and internal flows using four classical benchmark cases. Finally, the proposed explicit IBM for Neumann boundary condition is applied to a three-dimensional TFSI problem with moving boundary.

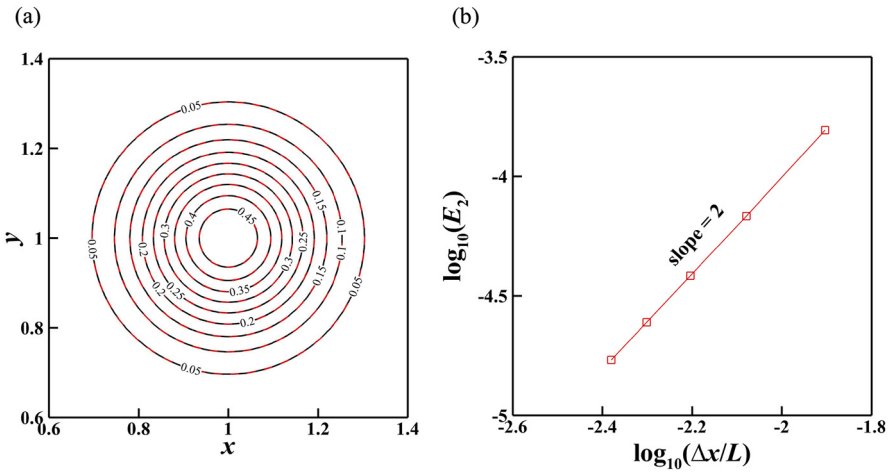

Fig. 3. (a) Comparison of the isotherms of simulated results (red solid line) and analytical solution (black dash line) at $F_o = 0.005$.(b) Convergence of numerical error versus mesh spacing for unsteady heat diffusion of a Gaussian hill, indicating that the overall accuracy of the proposed method is of second-order.

4.1. Numerical test of overall accuracy

Previous studies [13,19,33,34] have used two-dimensional decaying vortex flow, where a circular cylinder is immersed in the computational domain with analytical solution being imposed on the solid boundary, to analyze the stability and the convergence of IBM with Dirichlet boundary condition.

Similarly, we used the transient heat diffusion of a Gaussian hill with analytical temperature gradient being imposed on the solid boundary to examine the overall accuracy of the proposed explicit boundary condition-enforced IBM for Neumann boundary condition integrated with RTLBFS, where the analytical temperature gradient is imposed on the solid boundary. The numerical test is conducted on a 2D square computational domain with a side length of $2L$ and the periodic boundary condition is applied on the domain boundaries. A circular cylinder with a radius of $0.25L$ is placed at the center (L, L) of the uniformly discretized computational domain. The local temperature gradients on the solid boundary are obtained through the local analytical temperature as follows:

$$\frac{\partial T^k}{\partial n} = \frac{1}{2h}\left(T_O^{k,exact} - T_I^{k,exact}\right), \tag{40}$$

where the superscript "*exact*" denotes the analytical solution. In this test, the initial velocity field is set as $\mathbf{u} = (u_0, 0)$ and the initial temperature field is distributed with a Gaussian distribution:

$$T(\mathbf{x}, 0) = \frac{T_{ref}}{2\pi\sigma^2}\exp\left[\frac{-(\mathbf{x}-\mathbf{X}_c)^2}{2\sigma^2}\right], \tag{41}$$

where T_{ref} is the reference temperature and σ is a constant. The center of the Gaussian hill is represented by $\mathbf{X_c}$. The parameters $\sigma = 0.05L$, $T_{ref} = 2\pi\sigma^2$, and $\mathbf{X}_c = (0.5L, 0)$ are adopted. The analytical solution of the temperature field is characterized by:

$$T(\mathbf{x}, t) = \frac{T_c}{2\pi\left(2\chi t + \sigma^2\right)}\exp\left[\frac{-(\mathbf{x}-\mathbf{X}_c-\mathbf{u}t)^2}{2\left(2\chi t + \sigma^2\right)}\right]. \tag{42}$$

To examine the numerical accuracy of the proposed explicit boundary condition-enforced IBM for Neumann boundary condition, 5 different uniform meshes with mesh spacing of 80^2, 120^2, 160^2, 200^2, and 240^2 are applied to investigate the convergence order. The parameters $\Delta t = 1$ and $Pe = u_0 L/\chi = 100$ are adopted in each test. The relative error E_2 quantified by L_2 norm is calculated at $F_o = t\chi/L^2 = 0.005$ through the following expression:

$$E_2 = \sqrt{\frac{\sum_{i=1}^{N}\left(T^{numerical} - T^{exact}\right)^2}{N}}, \tag{43}$$

where the superscript "*numerical*" denotes the numerical results and N is the total grid number on the Eulerian mesh. Comparison of the isotherms of the numerical result obtained from the proposed method and the analytical solution obtained through Eq. (3) is shown in Fig. 3(a), where excellent agreement between the predicted results by the proposed method

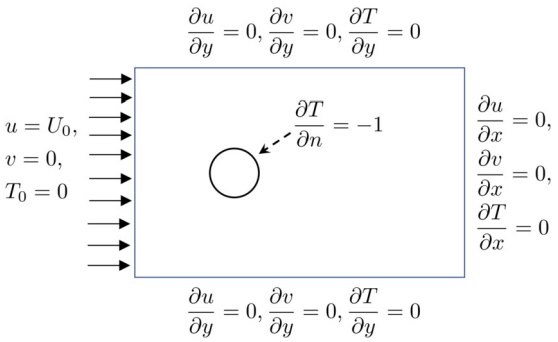

Fig. 4. Overview of the computational setup of an iso-heat-flux circular cylinder in a free stream.

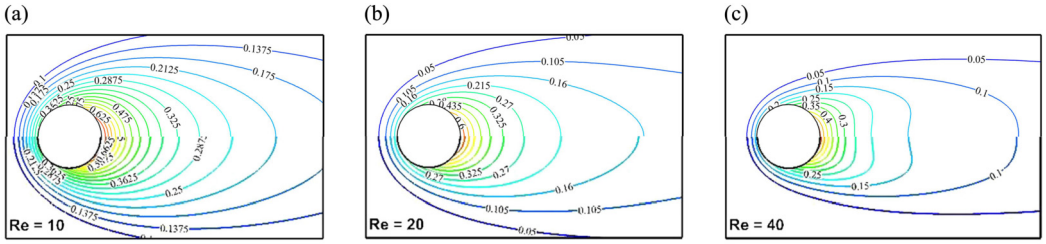

Fig. 5. Comparisons between isotherms of the mixed heat transfer from a heated circular cylinder with constant heat flux provided by Wang et al. [1] (lower part of each figure) and the present results (upper part of each figure) at three different Reynolds numbers, namely, (a) $Re = 10$, (b) $Re = 20$, and (c) $Re = 40$.

and the analytical solution is observed. It is evident from Fig. 3(b) that the overall accuracy of the proposed method is of second-order in space, demonstrating that the proposed explicit IBM for Neumann boundary condition has negligible effects on the global accuracy of the RTLBFS.

4.2. Forced convection around an iso-heat-flux circular cylinder

In this subsection, the mixed heat transfer around an iso-heat-flux cylinder is adopted to examine the suitability of the proposed explicit IBM for Neumann boundary condition in external flows. The problem is governed by two dimensionless parameters: the Reynolds number (Re) and the Prandtl number (Pr), which are defined as:

$$Re = \frac{U_0 D}{\nu}, \tag{44a}$$

$$Pr = \frac{\nu}{\chi}, \tag{44b}$$

respectively. U_0 is the flow velocity of the free stream and D denotes the diameter of the heated circular cylinder. In this numerical test, the Prandtl number is fixed at $Pr = 0.7$ and three Reynolds numbers are chosen, namely, 10, 20, and 40. At the surface of the cylinder, no-slip condition and iso-heat-flux condition ($\partial T/\partial n = -1$) are satisfied. The computational setup is shown in Fig. 4, where the free stream velocity $U_0 = 0.1$ and constant temperature of $T_0 = 0$ are applied on the left boundary and Neumann boundary condition is utilized on other boundaries. The local Nusselt number Nu_{local} and average Nusselt number $\overline{Nu}$ for measuring the heat transfer rate on the surface of solid boundary are defined as:

$$Nu_{local} = -\left(\frac{\partial T}{\partial n}\right)\frac{D}{T - T_0}, \tag{45a}$$

$$\overline{Nu} = \frac{1}{\pi D}\sum Nu_{local} \cdot \Delta s, \tag{45b}$$

respectively. In addition, the computational domain is set as $[-14D, 20D] \times [-15D, 15D]$ with a mesh size of 380×360, where the flow region around the iso-heat-flux cylinder $[-1.1D, 1.1D] \times [-1.1D, 1.1D]$ is discretized uniformly with a mesh spacing of $h = 0.01D$.

Fig. 5 shows the comparisons for the isotherms around the iso-heat-flux circular cylinder provided by Wang et al. [1] and the present results at three different Reynolds numbers. It can be seen that the predicted results by the proposed explicit IBM for Neumann boundary condition agree well with that of Wang et al. [1]. The present results are in consistent

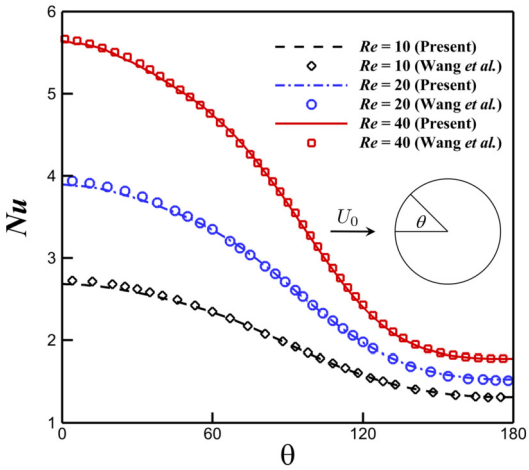

Fig. 6. The comparisons of the distribution of the local Nusselt number on the cylinder surface at different Reynolds numbers.

Table 3
Comparisons of the averaged Nusselt number $\overline{Nu}$ for flows past an iso-heat-flux cylinder at different Reynolds numbers.

Re	$\overline{Nu}$			
	Present	Ren et al. [28]	Wang et al. [1]	Ahmad and Qureshi [35]
10	**1.993**	2.016	2.01	2.041
20	**2.694**	2.741	2.69	2.662
40	**3.654**	3.741	3.68	3.472

with previous studies [1,28], qualitatively demonstrating the capability of the proposed explicit IBM for Neumann boundary condition to simulate the heat transfer with iso-heat-flux conditions in external flows.

In addition, quantitative comparisons of the local and averaged Nusselt numbers are performed to further evaluate the accuracy and capability of the proposed explicit IBM for NBC. Fig. 6 shows the local Nusselt number on the cylinder surface. It is evident from Fig. 6 that the present results are in good agreement with previous work of Wang et al. [1], indicating the feasibility of the proposed explicit IBM for NBC. In addition, as shown in Fig. 6, the local Nusselt number reaches its maximum value at the windward point and minimum point at the leeward point, indicating that the convection strength at windward point is much stronger than leeward point. Furthermore, the averaged Nusselt numbers tabulated in Table 3 for different Reynolds numbers are in excellent agreement with previous studies [1,28,35].

The local temperature gradients on the cylinder surface from the present study, Ren et al. [28], and theoretical analysis are provided in Fig. 7. It can be seen that the proposed explicit IBM for NBC agrees well with the prescribed theoretical value. The small discrepancies observed between the proposed method and theoretical value are due to the approximation relationships described in Eq. (38). Therefore, the proposed method can satisfy the NBC with high computational efficiency. Meanwhile, Fig. 7 shows that the temperature gradients of Ren et al. [28] deviate significantly from the theoretical value. Wang et al. [1] attributed the observed discrepancies in Ren et al. [28] to the one step explicit correction based IBMs, as these methods allow correct temperature on the solid boundary, but they don't satisfy the NBC due to the mutual interaction between temperature correction on the Eulerian grids and the heat source on Lagrangian points.

4.3. Forced convection around a moving iso-heat-flux circular cylinder

IBM has been widely adopted to investigate the complex TFSI problems with moving object, but the moving boundary could induce the accuracy degradation and the spurious force oscillations (SFO) for many IBMs. In this subsection, to evaluate the overall accuracy of the proposed method for moving boundary problems and examine whether the SFO appears in the present method, a circular cylinder moving with constant velocity of U_0 in the stationary fluid at $Re = U_0 D/\nu = 40$ and $Pr = \nu/\chi = 0.7$ is considered. The numerical test is performed on the domain of $[-10D, 10D] \times [-10D, 10D]$, where the moving region $[-6D, 6D] \times [-1.1D, 1.1D]$ is discretized by uniform mesh. The computational setup is shown in Fig. 8, in which the moving cylinder moves forward from $(5D, 0)$.

The test case is conducted on five different grids, where the moving region is discretized uniformly with mesh spacing of $D/80$, $D/100$, $D/120$, $D/140$ and $D/200$. The numerical results obtained with the finest grid 2500×560 (where the grid spacing of the moving region is $D/200$) are used as the reference solution. The relative errors E_2 are evaluated when the displacement of the cylinder achieves $10D$, which is defined as:

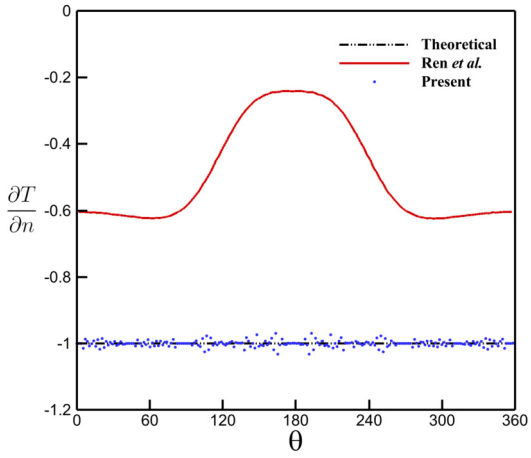

Fig. 7. Comparison of temperature gradient on the surface of the heated cylinder with constant heat flux at $Re = 20$.

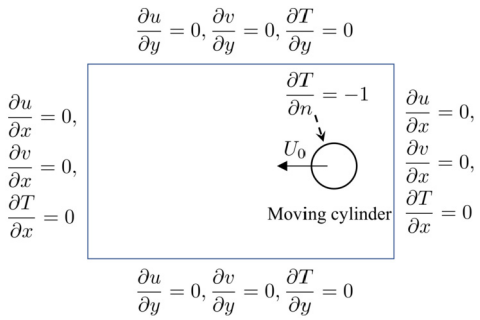

Fig. 8. The computational setup of a moving cylinder with constant moving velocity in the stationary fluid at $Re = 40$.

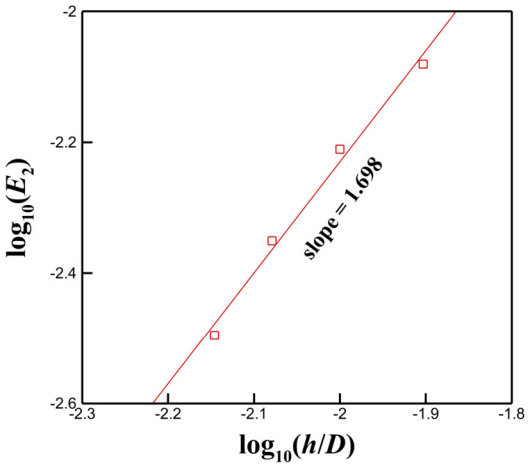

Fig. 9. Convergence of numerical error versus mesh spacing for a moving cylinder in the stationary fluid.

$$E_2 = \sqrt{\frac{\sum_{i=1}^{N} \left\| T_i^{numerical} - T_i^{reference} \right\|^2}{\sum_{i=1}^{N} \left\| T_i^{reference} \right\|^2}}. \tag{46}$$

Fig. 9 indicates that the overall accuracy of the proposed method for moving boundary problems is slightly lower than 2. It may be that the first-order smooth Dirac delta function shows stronger impact on the overall accuracy in moving problems. Fig. 10(a) shows the comparisons of the local Nusselt number distributions on the immersed boundary between the fixed cylinder and moving cylinder. It can be seen that the local Nusselt number distributions on the immersed boundary of

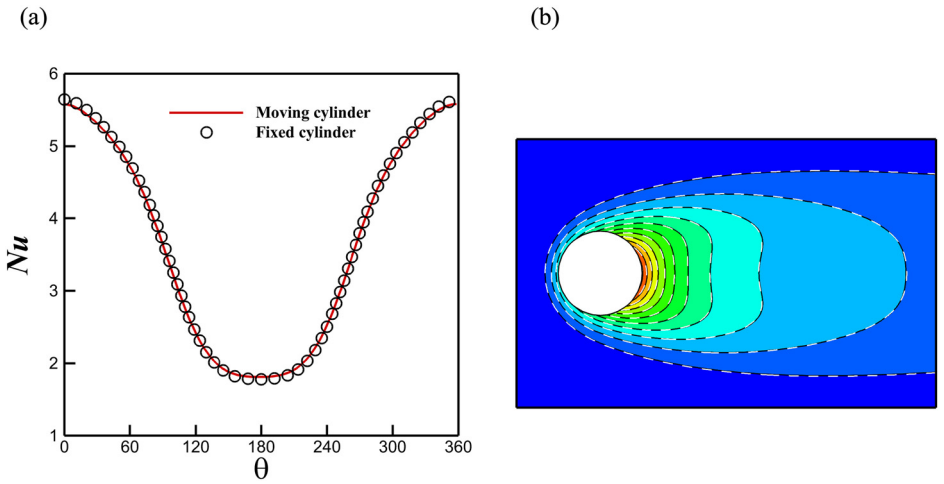

Fig. 10. Comparisons of (a) the local Nusselt number distributions on the immersed boundary and (b) temperature contours (background contour: fixed cylinder; white dotted lines: moving cylinder) between the fixed cylinder and the moving cylinder. The results of moving cylinder are generated by the mesh with the spatial resolution of $h = 0.01D$.

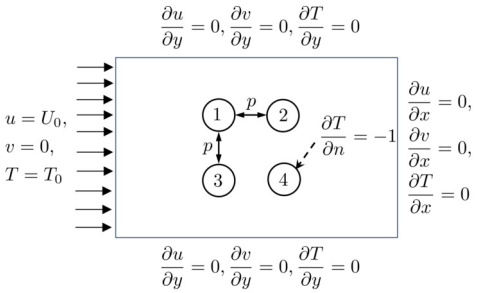

Fig. 11. The computational setup for four iso-heat-flux cylinders array in a free stream, where p denotes the distance between two cylinders.

the moving cylinder agree well with that of the fixed cylinder and very smooth without SFO. The comparisons of temperature contours (see Fig. 10(b)) further demonstrate that the temperature fields generated in the moving case are the same as the fields of the fixed cylinder and have no SFO. These results demonstrate that the proposed explicit IBM for Neumann boundary conditions is suitable for simulating TFSI problems with moving objects.

4.4. Forced convection around four iso-heat-flux cylinders array

In this subsection, the mixed heat transfer around four cylinders array in a square arrangement is adopted to examine the ability of the proposed method for simulating TFSI problems with multiple objects. Similarly, the problem is governed by the Reynolds number ($Re = U_0 D/\nu$), the Prandtl number ($Pr = \nu/\chi$) and the gap ratio (p/D). The computational setup of this test is shown in Fig. 11, where the boundary conditions on the cylinder's surface and domain boundaries are specified. The domain size of this test is set as $[-50D, 50D] \times [-15D, 15D]$, where the region around the cylinders array $[-3D, 3D] \times [-3D, 3D]$ is discretized uniformly with a mesh spacing of $h = 0.01D$.

In this numerical test, the parameters $Re = 40$ and $Pr = 0.7$ are adopted, and three gap ratios are adopted to investigate the effects of gap ratio on the heat transfer performance, namely, 0.5, 0.75, and 1. Fig. 12 shows the temperature contours and streamlines around the four cylinders array at different gap ratios. As shown in Fig. 12(a), (b) and (c), it can be seen that the temperature fields predicted by the proposed explicit IBM for Neumann boundary conditions agree well with the results generated by the original implicit IBM [1], which qualitatively demonstrating the capability of the proposed explicit IBM for Neumann boundary conditions to simulate the TFSI problems with multiple objects. In addition, with the increase of gap ratio, the temperature in the streamwise-gaps and lateral-gaps shows a significant reduction due to the enhancement of the gap flows.

To further evaluate the accuracy and capability of the proposed explicit IBM for Neumann boundary conditions, the comparisons of the local Nusselt number distributions on the four cylinders' surface between the proposed explicit IBM and the original implicit IBM [1] are performed in Fig. 13. It is evident from Fig. 13 that the results generated by the proposed explicit IBM are in good agreement with the results predicted by the original implicit IBM [1], demonstrating that the proposed explicit IBM can provide similar accuracy to the original implicit IBM [1] for TFSI problems with multiple objects.

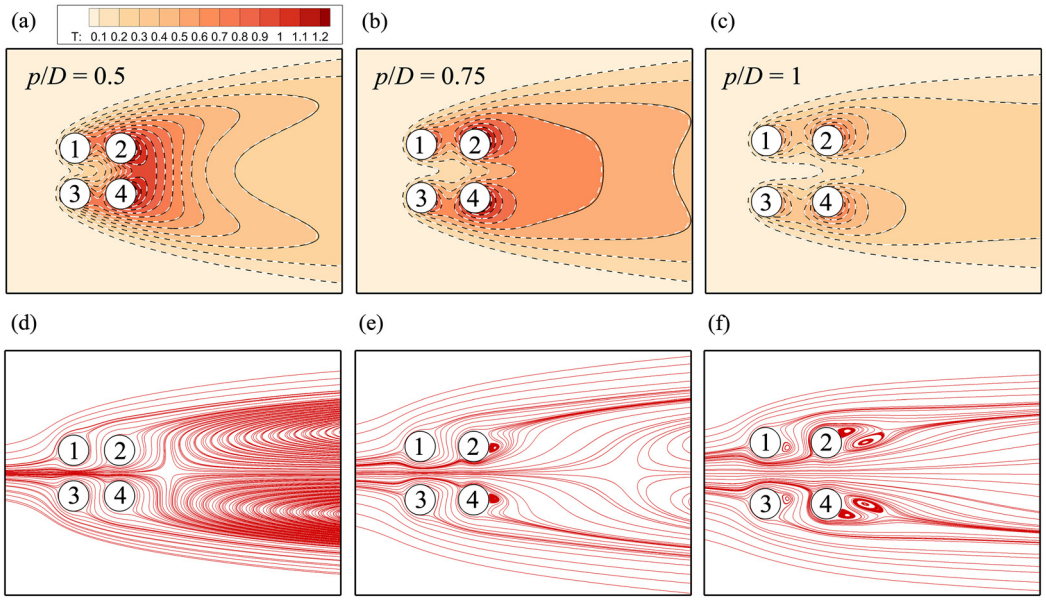

Fig. 12. The temperature fields (top row) and streamlines (bottom row) around the four cylinders array at different gap ratios. In the temperature fields, the background contours are predicted by the proposed explicit IBM and the white dotted lines denote the results generated by the original implicit IBM [1].

4.5. Mixed convection in a lid-driven cavity with an insulated cylinder

In this subsection, the mixed heat transfer around an insulated cylinder in a lid-driven cavity is adopted to examine the suitability of the proposed explicit IBM for Neumann boundary condition in internal flows. The computational setup and boundary conditions are shown in Fig. 14, where an insulated cylinder with a radius of $0.2L$ is placed at the center $(0.5L, 0.5L)$ of the square cavity. The top wall of the cavity has a constant horizontal velocity $U_0 = 0.1$ and a lower temperature $T_l = 0$; the bottom wall of the cavity is fixed with a higher temperature $T_h = 1$; two adiabatic lateral walls are fixed. This problem is governed by the following dimensionless group: the Reynolds number (Re), the Rayleigh number (Ra), the Prandtl number (Pr), and the Richardson number (Ri), which are defined as:

$$Re = \frac{U_0 L}{\nu}, \tag{47a}$$

$$Pr = \frac{\nu}{\chi}, \tag{47b}$$

$$Ra = \frac{\zeta g \left(T_h - T_l\right) L^3}{\nu \chi}, \tag{47c}$$

$$Ri = \frac{Ra}{Re^2 Pr}, \tag{47d}$$

respectively. In this numerical test, the parameters $Re = 100$ and $Pr = 0.7$ are adopted, and three typical Richardson numbers are chosen to investigate the effects of the buoyancy force, namely, 0.01, 1, and 10. In addition, the computational domain is discretized uniformly with a mesh size of 200×200, where the mesh spacing is $h = 0.005L$.

Fig. 15 shows the comparisons between the streamlines and the isotherms of an insulated circular cylinder in a lid-driven cavity provided by Wang et al. [1] and the present results at three different Richardson numbers. It can be seen that the results obtained by the proposed explicit IBM for NBC agree well with that of Wang et al. [1]. With the increase of the Richardson number, the large vortex over the cylinder (generated at $Ri = 0.01$) is suppressed at $Ri = 1$ and disappear at $Ri = 10$. This is because as Richardson number increases, the natural convection emerges and stabilizes the flow. It is worth mentioning here that the isotherms around the cylinder are perpendicular to the solid boundary, indicating that the NBC is satisfied on the cylinder surface. These results qualitatively demonstrate the capability of the proposed method for imposing the Neumann boundary condition.

The local Nusselt number along the bottom wall and temperature profile along the lateral line $x = 0.15L$ are compared with previous work [1] in Fig. 16 at different Richardson numbers to further quantitatively evaluate the accuracy and robustness of the proposed explicit IBM for NBC. It is evident from Fig. 16 that the present results agree well with the reference data from Wang et al. [1], demonstrating that the flow field obtained by the proposed explicit IBM is almost identical to that generated by the implicit IBM [1]. In addition, the temperature on the cylinder surface is compared with

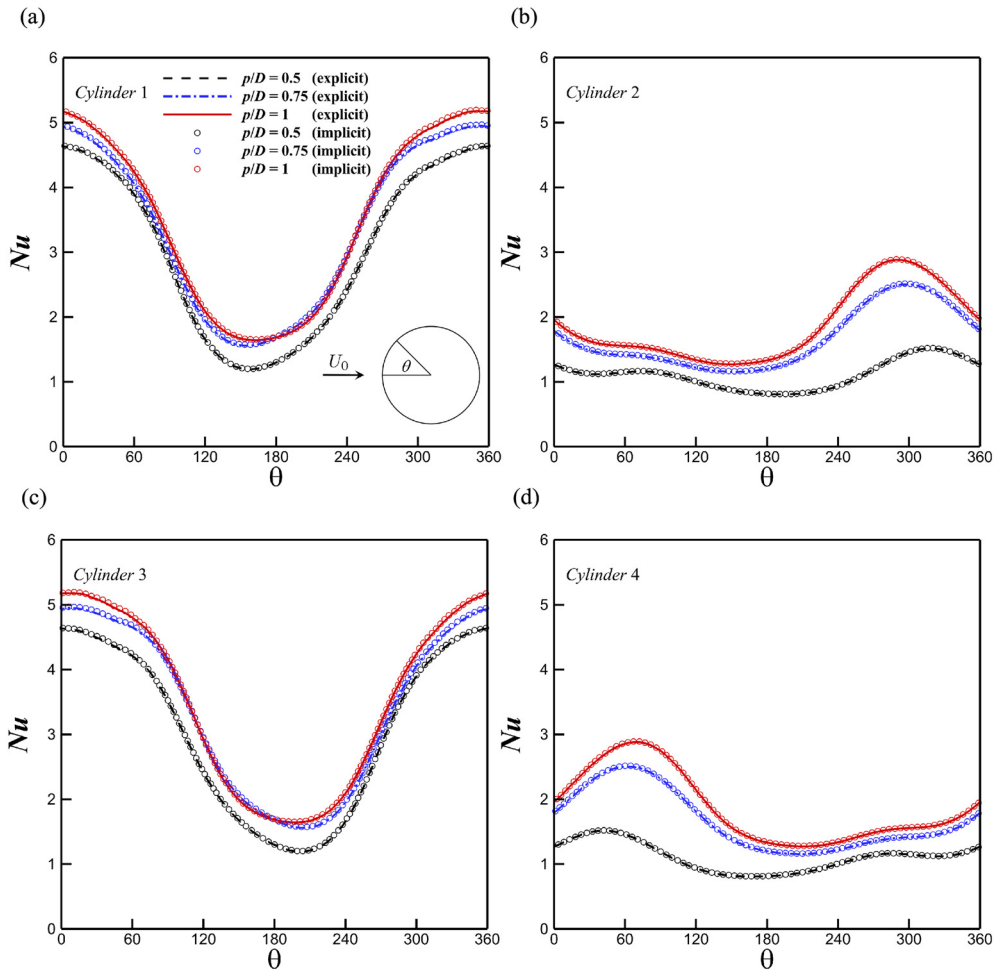

Fig. 13. The distributions of the local Nusselt number on the four cylinders' surface at different gap ratios, where the lines denote the results predicted by the proposed explicit IBM and the circles represent the results generated by the original implicit IBM [1].

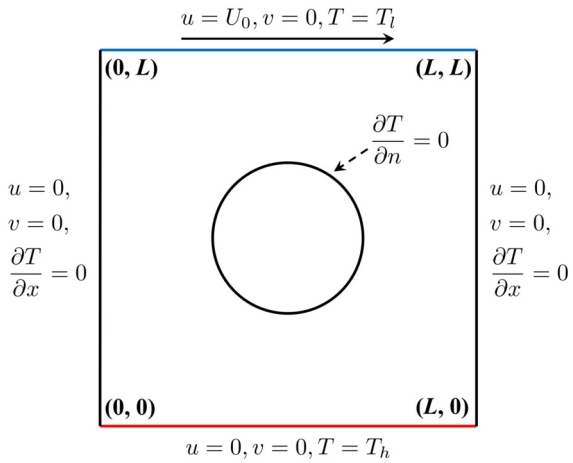

Fig. 14. Scheme of the computational setup for an insulated cylinder located in a lid-driven cavity.

the previous work [1] in Fig. 17. It can be seen that the present computational results on the cylinder surface are in good agreement with the results generated by the original implicit IBM [1].

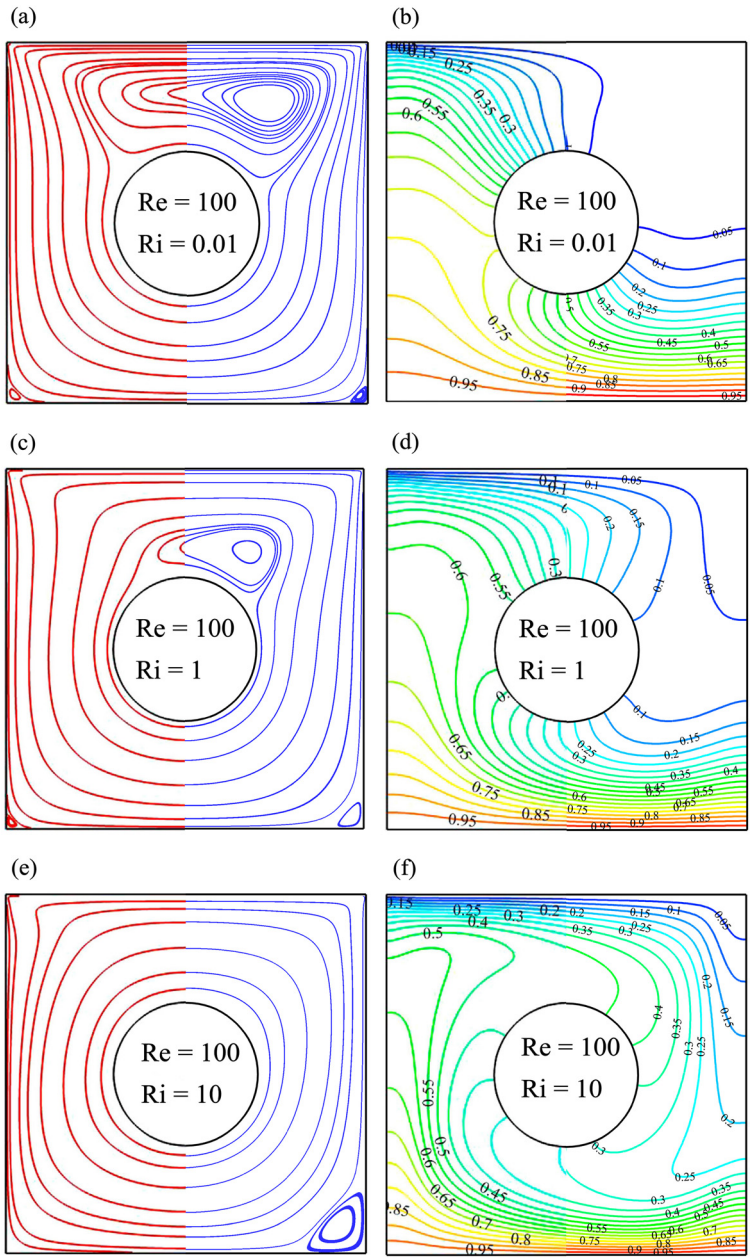

Fig. 15. Comparisons between streamlines (left column) and isotherms (right column) of the mixed heat transfer around an insulated cylinder in a lid-driven cavity provided by Wang et al. [1] (left part of each figure) and the present results (right part of each figure) at $Re = 100$ and three different Richardson numbers, namely, $Ri = 0.01$ (top row), $Ri = 1$ (middle row), and $Ri = 10$ (bottom row).

To quantitatively validate whether the temperature field around the cylinder satisfies the Neumann boundary condition, the temperature gradient on the cylinder surface is presented in Fig. 18. It can be seen that the Neumann boundary condition is achieved on the cylinder surface. The approximation relationship of Eq. (38) indicates that the error of the temperature gradient on the solid wall is $O(h)$. These results demonstrate that the proposed explicit IBM successfully impose the Neumann boundary condition on the solid wall.

4.6. Mixed convection around an iso-heat-flux rotating sphere in a cubic enclosure

The capability of the proposed explicit IBM for NBC to capture the dynamic response of 3D moving boundary problems is assessed on a 3D problem involving mixed convection around a vertical rotating sphere with iso-heat-flux in a cubical enclosure.

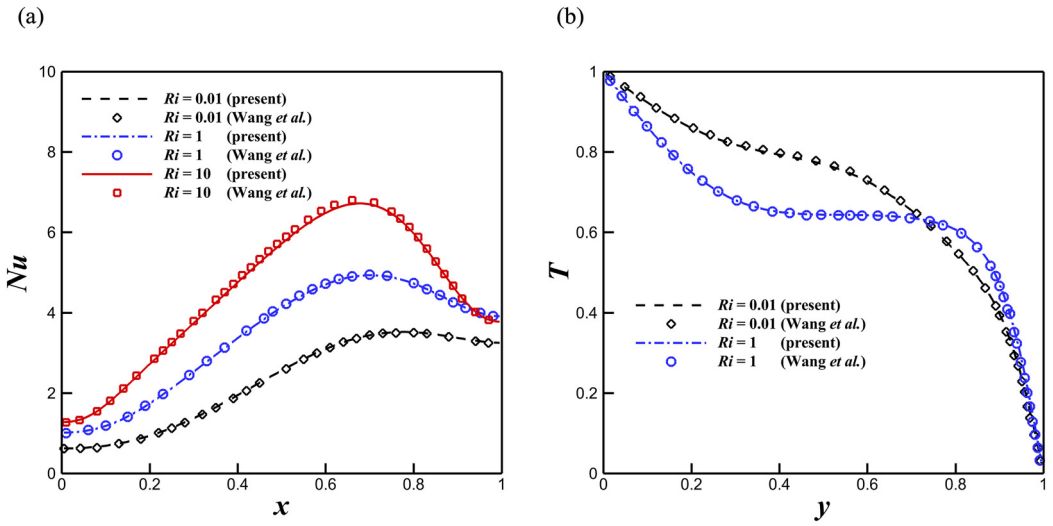

Fig. 16. Comparisons of (a) local Nusselt number at $y = 0$ and (b) local temperature at $x = 0.15L$ for mixed heat transfer around an insulated cylinder in a lid-driven cavity at three different Richardson numbers.

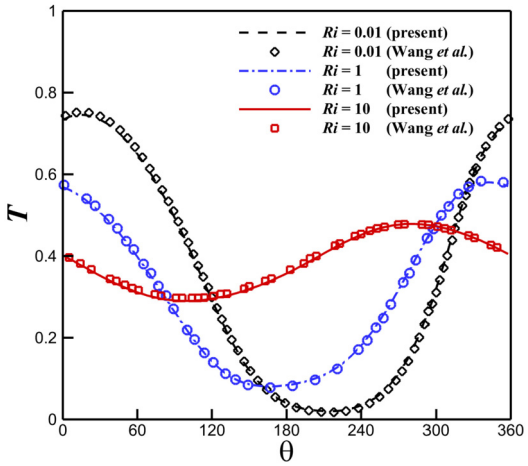

Fig. 17. Comparisons of temperature on the cylinder surface at three different Richardson numbers.

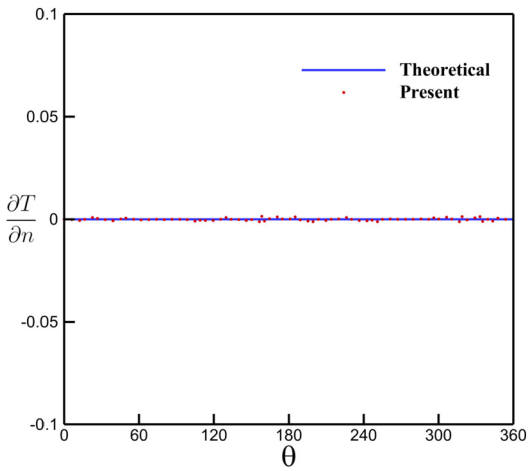

Fig. 18. The temperature gradient on the cylinder surface of the mixed heat transfer around an insulated cylinder in a lid-driven cavity.

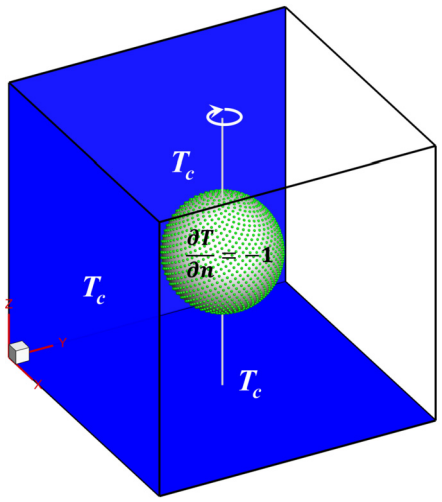

Fig. 19. Scheme of the computational setup for mixed convection around a heated rotating sphere in a concentric cubical enclosure, where the no-slip condition and lower temperature ($T_c = 0$) are imposed on the six walls of the cubic enclosure and the iso-heat-flux boundary condition ($\partial T/\partial n = -1$) is applied on the solid boundary. The green points denote the distributed Lagrangian points and the rotating axis is along the z-direction.

Fig. 19 shows the computational setup for mixed convection around an iso-heat-flux sphere in a cube of length L, where the iso-heat-flux sphere ($\partial T/\partial n = -1$) with radius $r = 0.2L$ is located at the domain center. The no-slip condition and constant lower temperature ($T_c = 0$) are imposed on all six walls. This problem is governed by the following dimensionless group: the rotational Reynolds number Re_w, the Rayleigh number Ra, and the Prandtl number Pr, which are defined as:

$$Re_w = \frac{\omega r L}{\nu}, \tag{48a}$$

$$Ra = \frac{\zeta g Q L^4}{\nu \chi^2} = \frac{U_0^2 L^2}{\nu \chi}, \tag{48b}$$

$$\mathrm{Pr} = \frac{\nu}{\chi}, \tag{48c}$$

where ω denotes the rotational speed and $Q = -\chi \partial T/\partial n$ is the heat flux. $U_0 = \sqrt{\frac{\zeta g Q L^2}{\chi}}$ is defined as the characteristic velocity, which should satisfy the low Mach number limitation. The averaged temperature in the buoyancy force is defined as $T_m = T_c$. In the present test, the Rayleigh number and the Prandtl number are set as $Ra = 10^5$ and $Pr = 0.7$, respectively. The rotational Reynolds number is varied from 0 to 300 with an interval of 50. In this test, a uniform Cartesian mesh with the size of 200^3 is adopted. To distribute the Lagrangian points (green points in Fig. 19) evenly on the spherical surface, the position of each Lagrangian point is defined by the Fibonacci lattice [36], which can be expressed as:

$$\begin{aligned} \varphi &= \frac{2n-1}{N} - 1, \quad \xi = \frac{\sqrt{5}-1}{2}, \\ (x_n, y_n, z_n) &= \left(r\sqrt{1-\varphi^2}\cos(2\pi n\xi), r\sqrt{1-\varphi^2}\sin(2\pi n\xi), r\varphi \right), \end{aligned} \tag{49}$$

where n is the index of each Lagrangian point, N denotes the total number of the Lagrangian points, and ξ is the golden ratio. The position of the auxiliary points on the two auxiliary layers is determined with the same method. In this test, the ratio of the maximum distance between adjacent Lagrangian points to the Eulerian mesh spacing should be less than 1.6 to establish a proper correlation between Lagrangian points and Eulerian meshes; thereby, the total number of Lagrangian points is set as 10^4 in this study.

The local Nusselt number Nu_{local} and the averaged Nusselt number $\overline{Nu}$ on the spherical surface are defined as:

$$Nu_{sp} = -\left(\frac{\partial T}{\partial n}\right)\frac{L}{T - T_c}, \tag{50a}$$

$$\overline{Nu_{sp}} = \frac{1}{4\pi r^2}\sum Nu_{sp} \cdot \Delta s, \tag{50b}$$

respectively.

To fairly evaluate the Nusselt number on the six cold walls, $T_{ref} = 1$ is introduced to nondimensionalize the temperature gradient. Thereby, the local Nusselt number and the averaged Nusselt number on the walls are defined as

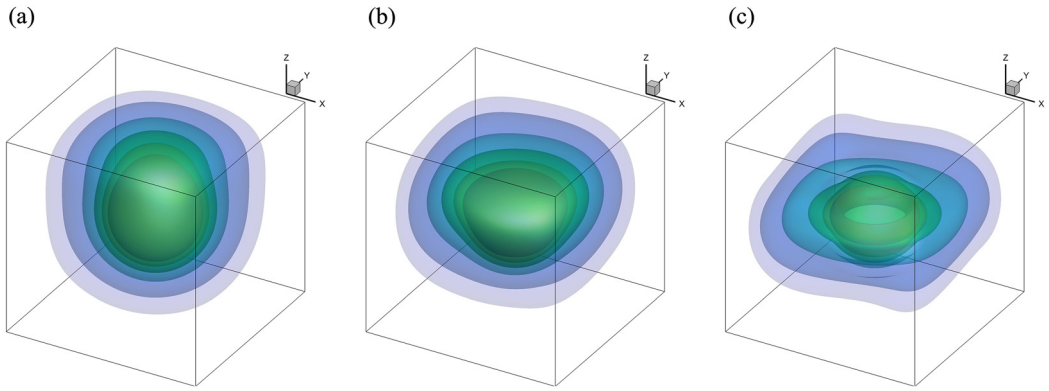

Fig. 20. 3D isosurfaces of the mixed convection between an iso-heat-flux rotating sphere and outer cubic cavity at three rotational Reynolds numbers: (a) $Re_w = 0$, (b) $Re_w = 150$, (c) $Re_w = 300$.

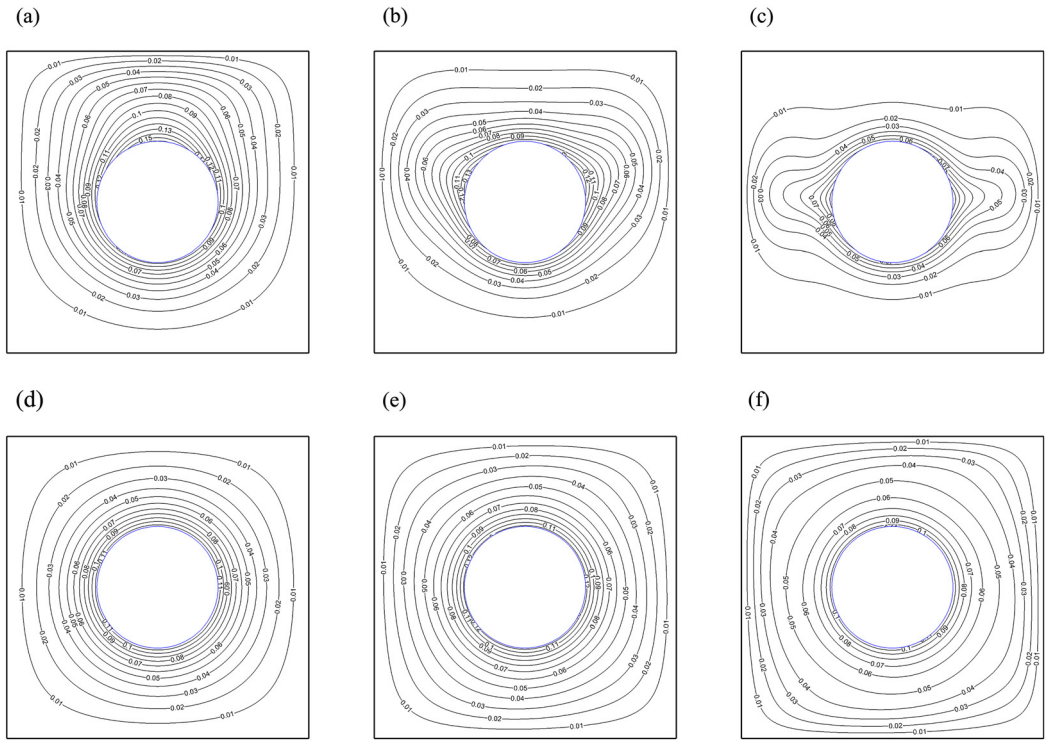

Fig. 21. The isotherms on the x-mid (top row) and z-mid (bottom row) planes of the mixed convection between an iso-heat-flux rotating sphere and outer cubic cavity at three rotational Reynolds numbers: (a, d) $Re_w = 0$, (b, e) $Re_w = 150$, (c, f) $Re_w = 300$.

$$Nu_{local} = -\left(\frac{\partial T}{\partial n}\right)\frac{L}{T_{ref} - T_c}, \tag{51a}$$

$$\overline{Nu} = \frac{1}{L^2}\sum Nu_{local} \cdot \Delta s. \tag{51b}$$

Fig. 20 shows the 3D iso-surfaces around the iso-heat-flux sphere at three different rotational Reynolds numbers. Comparing with the stationary case ($Re_w = 0$, see Fig. 20(a)), the rotating behavior induces the expansion of the isotherms in the radial direction, which implies that the heat transfer rate is enhanced. To clearly evaluate the effects introduced by the rotating behavior on the temperature distribution in the cavity, the isotherms on the x-mid and z-mid planes are presented in Fig. 21. As the rotational Reynolds number increases, the dominant component controlling the flow patter transits from natural convection to rotational behavior. When the flow pattern is dominated by the natural convection, the isotherms are stretched along the z direction; when the centrifugal motion becomes the leading character, the isotherms on the x-mid and z-mid plane are stretched in the horizontal plane, which is induced by the rotational behavior generating the extra centrifugal transport behavior of the fluid.

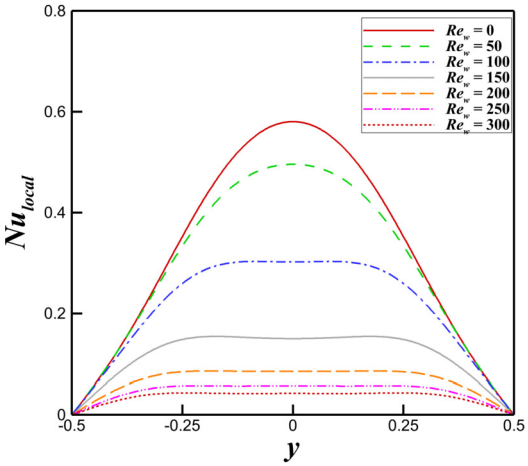

Fig. 22. The comparisons of the distribution of the local Nusselt number on the top edge of the x-mid plane at different rotational Reynolds numbers.

Table 4
Comparisons of the averaged Nusselt number on the six walls and the spherical surface at different rotational Reynolds numbers.

Re_w	$\overline{Nu_{sp}}$	$\overline{Nu_S}$	$\overline{Nu_T}$	$\overline{Nu_B}$
0	8.4000	0.0726	0.1906	0.0383
50	8.3825	0.0756	0.1801	0.0365
100	8.4289	0.0859	0.1431	0.0323
150	8.9448	0.1008	0.0876	0.0282
200	9.9908	0.1102	0.0528	0.0251
250	11.1502	0.1149	0.0370	0.0227
300	12.2544	0.1174	0.0289	0.0207

Table 5
Comparisons of the averaged Nusselt number on the six walls and the spherical surface between the explicit and implicit IBMs at $Re_w = 300$.

Algorithm	$\overline{Nu_T}$	$\overline{Nu_B}$	$\overline{Nu_S}$	$\overline{Nu_{sp}}$
Explicit IBM	0.0289	0.0207	0.1174	12.2544
Implicit IBM	0.0290	0.0207	0.1172	12.2763
Relative difference	0.345%	0	0.171%	0.178%

To quantitatively analyze the effects introduced by the rotating behavior, the local and averaged Nusselt numbers are presented. Fig. 22 shows the local Nusselt number on the top edge of the x-mid plane. It is evident from Fig. 22 that the local Nusselt number decreases with the increase of the rotational Reynolds number, indicating that the heat transfer rate is weakened along the vertical direction. The averaged Nusselt numbers on the spherical surface ($\overline{Nu_{sp}}$), the side walls ($\overline{Nu_S}$), the top wall ($\overline{Nu_T}$), and the bottom wall ($\overline{Nu_B}$) are tabulated in Table 4. It clearly shows that the heat transfer pattern transits from the natural convection mode to forced convection mode. The heat transfer rates on the top and bottom walls are decreased by approximately 85% and 46% at $Re_w = 300$, respectively, when being compared to the stationary case. On the other hand, the enhanced centrifugal motion increases the heat transfer rates on the side wall by approximately 162%. These results indicate that the rotational behavior redistributes the heat transfer rates of the cubic enclosure walls.

As described previously, the approximation relationship utilized in the proposed explicit IBM for NBC will introduce some high order errors in the temperature gradient. Therefore, further investigation into the isotherms along the x-mid plane and the distributions of temperature and temperature gradient on the spherical surface is performed to evaluate the influence of the approximation relation on the numerical results shown in Fig. 23. As shown in Fig. 23, the isotherms and the surface temperature generated by the proposed explicit IBM are in excellent agreement with the results obtained by the implicit IBM, albeit small fluctuations in the temperature gradient around the prescribed value. To further assess the accuracy of the explicit IBM in 3D TFSI problem with moving boundary, the averaged Nusselt number on the spherical surface and cavity walls are tabulated in Table 5. The relative differences between the results predicted by the explicit and implicit IBMs are very small, indicating that the proposed explicit IBM can provide similar accuracy to the original implicit IBM [1] for 3D TFSI problems.

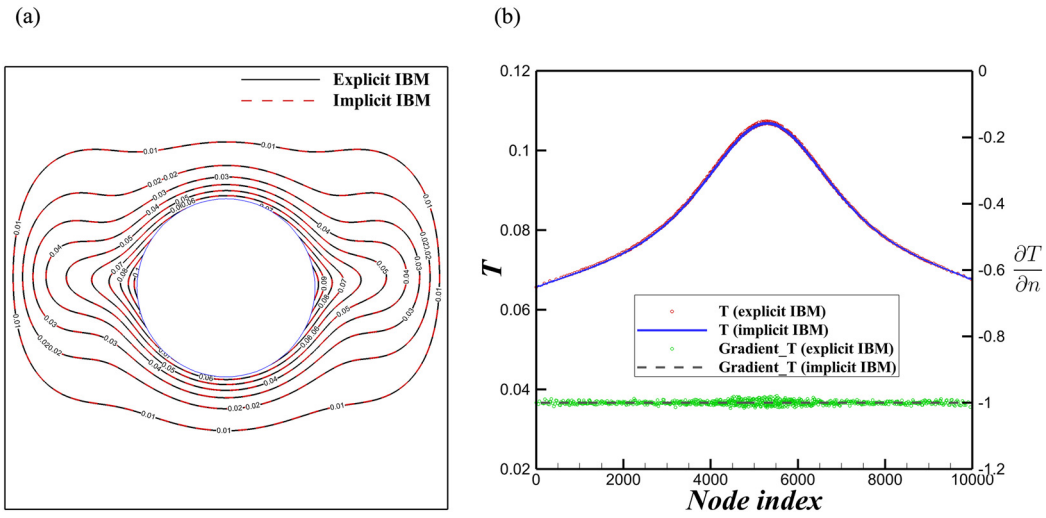

Fig. 23. (a) The comparisons of the isotherms on the x-mid plane between the explicit and implicit IBMs at $Re_w = 300$. (b) The comparisons of the temperature and its gradient distribution on the spherical surface between the explicit and implicit IBMs at $Re_w = 300$.

5. Conclusions

In this work, the explicit boundary condition-enforced immersed boundary method for Neumann boundary condition is proposed to eliminate the high computational cost and significant memory usage in the original implicit IBM, while maintaining similar accuracy to the implicit method. Based on the error analysis using Taylor series expansion, a second-order approximation can be obtained; with this approximation, the explicit IBM circumvent the needs to assemble a large correlation matrix and inverse it, which are intrinsic limitations in the original implicit boundary condition-enforced IBM. The explicit IBM is integrated with the reconstructed thermal lattice Boltzmann flux solver (RTLBFS) to solve the TFSI problems. The intermediate flow field without considering the existence of the solid body is predicted by the RTLBFS. Subsequently, the IBMs for Dirichlet boundary condition and Neumann boundary condition are introduced to simultaneously evaluate the velocity and temperature corrections.

The proposed numerical approach is validated with several benchmark cases, including the TFSI problems related to the external and internal flows. The numerical accuracy test indicates that the overall accuracy of the explicit IBM with RTLBFS is second-order accuracy on space. The good agreement between the numerical results generated by the explicit IBM and previous works further demonstrates the feasibility and robustness of the explicit IBM. Lastly, a three-dimensional mixed convection around an iso-heat-flux rotating sphere in a cubic enclosure is considered, where 10^4 Lagrangian points are involved. The results show that the relative difference between the explicit and implicit IBMs is almost negligible and the capability of the explicit IBM for three-dimensional moving boundary TFSI problem with Neumann boundary condition is on par with the original implicit IBM. Hence, these results demonstrate that the proposed explicit boundary condition-enforced IBM is capable of providing identical accuracy as to implicit IBM at only a fraction amount of computational resources, allowing the proposed method to be deployed for complex TFSI problems involving NBC. Similar to the boundary condition-enforced IBM for Dirichlet boundary conditions [13,23], the proposed explicit IBM for Neumann boundary conditions can be easily integrated with LBM and N-S solvers to simulate TFSI problems.

Owing to the use of the outer auxiliary layer, the proposed method is not suitable for simulating very dense particle-fluid systems. The minimum distance between two objects should not be smaller than $1.5h$. Otherwise, the physical variables cannot be accurately evaluated.

CRediT authorship contribution statement

Buchen Wu: Conceptualization, Methodology, Software, Validation, Writing – original draft. **Jinhua Lu:** Methodology, Writing – original draft. **HsuChew Lee:** Writing – original draft. **Chang Shu:** Formal analysis, Supervision, Writing – original draft. **Minping Wan:** Formal analysis, Supervision, Writing – original draft.

Declaration of competing interest

The authors declare that they have no known competing financial interests or personal relationships that could have appeared to influence the work reported in this paper.

Data availability

The data of this study are available within the article.

Acknowledgements

This work has been supported by the Key-Area Research and Development Program of Guangdong Province (Grant No. 2021B0101190003), the Department of Science and Technology of Guangdong Province (Grant No. 2020B1212030001), and the Shenzhen Science & Technology Program (Grant No. KQTD20180411143441009). Numerical simulations have been supported by the Center for Computational Science and Engineering of Southern University of Science and Technology.

References

[1] Y. Wang, C. Shu, L. Yang, Boundary condition-enforced immersed boundary-lattice Boltzmann flux solver for thermal flows with Neumann boundary conditions, J. Comput. Phys. 306 (2016) 237–252.
[2] C.S. Peskin, Numerical analysis of blood flow in the heart, J. Comput. Phys. 25 (1977) 220–252.
[3] Z.-G. Feng, E.E. Michaelides, Robust treatment of no-slip boundary condition and velocity updating for the lattice-Boltzmann simulation of particulate flows, Comput. Fluids 38 (2009) 370–381.
[4] J. Mohd-Yusof, Combined immersed-boundary/B-spline methods for simulations of flow in complex geometries, Cent. Turbul. Res. Annu. Res. Briefs 161 (1997) 317–327.
[5] M. Uhlmann, An immersed boundary method with direct forcing for the simulation of particulate flows, J. Comput. Phys. 209 (2005) 448–476.
[6] J. Kim, D. Kim, H. Choi, An immersed-boundary finite-volume method for simulations of flow in complex geometries, J. Comput. Phys. 171 (2001) 132–150.
[7] E. Fadlun, R. Verzicco, P. Orlandi, J. Mohd-Yusof, Combined immersed-boundary finite-difference methods for three-dimensional complex flow simulations, J. Comput. Phys. 161 (2000) 35–60.
[8] N. Zhang, Z.C. Zheng, An improved direct-forcing immersed-boundary method for finite difference applications, J. Comput. Phys. 221 (2007) 250–268.
[9] D. Goldstein, R. Handler, L. Sirovich, Modeling a no-slip flow boundary with an external force field, J. Comput. Phys. 105 (1993) 354–366.
[10] X. Niu, C. Shu, Y. Chew, Y. Peng, A momentum exchange-based immersed boundary-lattice Boltzmann method for simulating incompressible viscous flows, Phys. Lett. A 354 (2006) 173–182.
[11] Y. Hu, H. Yuan, S. Shu, X. Niu, M. Li, An improved momentum exchanged-based immersed boundary–lattice Boltzmann method by using an iterative technique, Comput. Math. Appl. 68 (2014) 140–155.
[12] H.-Z. Yuan, X.-D. Niu, S. Shu, M. Li, H. Yamaguchi, A momentum exchange-based immersed boundary-lattice Boltzmann method for simulating a flexible filament in an incompressible flow, Comput. Math. Appl. 67 (2014) 1039–1056.
[13] J. Wu, C. Shu, Implicit velocity correction-based immersed boundary-lattice Boltzmann method and its applications, J. Comput. Phys. 228 (2009) 1963–1979.
[14] J. Wu, C. Shu, An improved immersed boundary-lattice Boltzmann method for simulating three-dimensional incompressible flows, J. Comput. Phys. 229 (2010) 5022–5042.
[15] Y. Wang, C. Shu, C. Teo, L. Yang, An efficient immersed boundary-lattice Boltzmann flux solver for simulation of 3D incompressible flows with complex geometry, Comput. Fluids 124 (2016) 54–66.
[16] Y. Wang, C. Shu, L. Yang, Y. Sun, On the immersed boundary-lattice Boltzmann simulations of incompressible flows with freely moving objects, Int. J. Numer. Methods Fluids 83 (2017) 331–350.
[17] Y. Wang, C. Shu, L. Yang, C. Teo, An immersed boundary-lattice Boltzmann flux solver in a moving frame to study three-dimensional freely falling rigid bodies, J. Fluids Struct. 68 (2017) 444–465.
[18] H. Yan, G. Zhang, Y. Xiao, D. Hui, S. Wang, A surface flux correction-based immersed boundary-multiphase lattice Boltzmann flux solver applied to multiphase fluids–structure interaction, Comput. Methods Appl. Mech. Eng. 400 (2022) 115481.
[19] X. Zhao, Z. Chen, L. Yang, N. Liu, C. Shu, Efficient boundary condition-enforced immersed boundary method for incompressible flows with moving boundaries, J. Comput. Phys. (2021) 110425.
[20] B. Wu, C. Shu, M. Wan, Y. Wang, S. Chen, Hydrodynamic performance of an unconstrained flapping swimmer with flexible fin: a numerical study, Phys. Fluids 34 (2022) 011901.
[21] B. Wu, C. Shu, H. Lee, M. Wan, The effects of caudal fin's bending stiffness on a self-propelled carangiform swimmer, Phys. Fluids 34 (2022) 041901.
[22] B. Wu, C. Shu, H. Lee, M. Wan, Numerical study on the hydrodynamic performance of an unconstrained carangiform swimmer, Phys. Fluids 34 (2022) 121902.
[23] W. Ren, C. Shu, J. Wu, W. Yang, Boundary condition-enforced immersed boundary method for thermal flow problems with Dirichlet temperature condition and its applications, Comput. Fluids 57 (2012) 40–51.
[24] Z. Chen, C. Shu, L. Yang, X. Zhao, N. Liu, Immersed boundary–simplified thermal lattice Boltzmann method for incompressible thermal flows, Phys. Fluids 32 (2020) 013605.
[25] Z. Chen, L. Yang, C. Shu, X. Zhao, N. Liu, Y. Liu, Mixed convection between rotating sphere and concentric cubical enclosure, Phys. Fluids 33 (2021) 013605.
[26] B. Wu, J. Lu, H. Lee, C. Shu, M. Wan, An explicit immersed boundary-reconstructed thermal lattice Boltzmann flux solver for thermal–fluid–structure interaction problems, Int. J. Mech. Sci. 235 (2022) 107704.
[27] N. Zhang, Z. Zheng, S. Eckels, Study of heat-transfer on the surface of a circular cylinder in flow using an immersed-boundary method, Int. J. Heat Fluid Flow 29 (2008) 1558–1566.
[28] W. Ren, C. Shu, W. Yang, An efficient immersed boundary method for thermal flow problems with heat flux boundary conditions, Int. J. Heat Mass Transf. 64 (2013) 694–705.
[29] Y. Hu, D. Li, S. Shu, X. Niu, Study of multiple steady solutions for the 2D natural convection in a concentric horizontal annulus with a constant heat flux wall using immersed boundary-lattice Boltzmann method, Int. J. Heat Mass Transf. 81 (2015) 591–601.
[30] Y. Hu, D. Li, S. Shu, X. Niu, An efficient immersed boundary-lattice Boltzmann method for the simulation of thermal flow problems, Commun. Comput. Phys. 20 (2016) 1210–1257.
[31] J. Lu, C. Dai, P. Yu, Analysis and reconstruction of the thermal lattice Boltzmann flux solver, Int. J. Numer. Methods Fluids (2022).
[32] J. Lu, H. Lei, C. Shu, C. Dai, The more actual macroscopic equations recovered from lattice Boltzmann equation and their applications, J. Comput. Phys. 415 (2020) 109546.

[33] L. Yang, C. Shu, W. Yang, Y. Wang, J. Wu, An immersed boundary-simplified sphere function-based gas kinetic scheme for simulation of 3D incompressible flows, Phys. Fluids 29 (2017) 083605.
[34] B. Wu, J. Lu, H. Lee, C. Shu, M. Wan, An efficient explicit immersed boundary-reconstructed lattice Boltzmann flux solver for isothermal fluid-structure interaction problems with large deformations and complex geometries, Appl. Math. Model. 114 (2023) 627–645.
[35] R. Ahmad, Z. Qureshi, Laminar mixed convection from a uniform heat flux horizontal cylinder in a crossflow, J. Thermophys. Heat Transf. 6 (1992) 277–287.
[36] Á. González, Measurement of areas on a sphere using Fibonacci and latitude–longitude lattices, Math. Geosci. 42 (2010) 49–64.